Submarine landslide morphometrics and slope failure dynamics along a mixed carbonate-siliciclastic margin, north-eastern Australia

Ángel Puga-Bernabéu [a,c,*], Javier López-Cabrera [b], Jody M. Webster [c], Robin J. Beaman [d]

[a] *Departamento de Estratigrafía y Paleontología, Universidad de Granada, 18002 Granada, Spain*
[b] *Irish Centre for Research in Applied Geosciences, University College Dublin, Belfield, Dublin 4, Ireland*
[c] *Geocoastal Research Group, School of Geosciences, The University of Sydney, NSW 2006, Australia*
[d] *College of Science and Engineering, James Cook University, PO Box 6811, Cairns, Queensland 4870, Australia*

ABSTRACT

Comparatively little work has been carried out on the morphology and distribution of submarine landslides on mixed carbonate-siliciclastic margins. The morphometric analysis of 84 open slope submarine landslides on the Great Barrier Reef (GBR) margin of north-eastern Australia provides useful insights into slope failure dynamics and frequency distribution of landslides on mixed margins. Our analysis has revealed that the slope area affected by failures (12.6% of the margin) is similar to siliciclastic-dominated passive margins, although the total volume of remobilized sediment (73 km^3) is comparatively small. Landslide scars lie at shallower depths to the south of the margin (mean of 576 m vs 1517 m to the north) and there is good correlation between the depth at origin and depth at termination for the GBR landslides. The cumulative frequency distribution of volume, area and total length of the GBR landslides does not fit to common distributions (e.g., power law, logarithmic or exponential) for the entire dataset. Still, the cumulative frequency distribution of landslide dimensions can be statistically explained either by a power law similar to other passive margins, or by a lognormal distribution similar to some siliciclastic margins. Morphometric characteristics, such as the volume of sediment released per unit width and the probability function of volume distribution suggest that slope failures mainly involved relatively unconsolidated sediments. We find that the disintegration by debris flows was the dominant process along the entire GBR margin and that their spreading efficiency and mobility was relatively low. Margin stratigraphy, fluid overpressure at the base of the slope, and detachment surfaces at the boundary between different lithologies that separate sedimentary cycles may have preconditioned the slope to fail. This compilation provides a robust morphometric framework that allows comparison with existing and future slope failure databases, and lays the foundation for performing numerical simulations to assess the landslide-generated tsunamigenic hazards along the GBR margin.

1. Introduction

Slope instabilities along continental margins are recorded by the presence of landslide scars and mass-transport deposits of dimensions that vary over several orders of magnitude (e.g., 1–10^5 km^2 of extent and 0.1–1000 km^3 of sediment volume; Bohannon and Gardner, 2004; Haflidason et al., 2004; Lastras et al., 2004b; Moscardelli and Wood, 2008; Chiocci and Casalbore, 2017). Large-scale submarine landslides have significantly modified continental margins during the Late Pleistocene and Holocene (Normark et al., 2004; Solheim et al., 2005; Owen et al., 2007; Lee, 2009; Dalla Valle et al., 2015) and thus, it is thought they might potentially impact offshore infrastructures, such as pipelines,

cables and hydrocarbon platforms (Nadim and Locat, 2005; Nadim, 2006). Additionally, their role in delivering shelf-edge and slope sediments to the deeper basins is comparable to that of turbidite systems (Prélat et al., 2010; Jobe et al., 2018). The interest of the hydrocarbon industry, together with the socioeconomic importance related to their tsunamigenic potential (Grilli et al., 2009; ten Brink et al., 2009b; Kawamura et al., 2014), has driven the increasing number of studies on submarine landslides over the last 30 years (see Masson et al., 2006 for a general overview). The first step in understanding the generation, evolution and triggering mechanisms of submarine landslides is their identification by geophysical techniques using high-resolution bathymetric and sub-seafloor data, and to perform morphometric analysis.

The most complete catalogue of slope failures in terms of morphometric characterization comes from the North Atlantic and adjacent seas, such as the Mediterranean Sea, which also include many of the best-studied submarine landslides worldwide (Canals et al., 2004; Hühnerbach et al., 2004; Chaytor et al., 2009; Twichell et al., 2009; Urgeles and Camerlenghi, 2013). Similar inventories are also available from the Pacific U.S. margin (McAdoo et al., 2000) and the margin of the Middle America Trench (Völker et al., 2016). However, comparable summaries are lacking in the western Pacific. Recently, Moscardelli and Wood (2016) presented a database for mass-transport deposits reported in a variety of margins worldwide, and that uses the external architecture of the deposits to establish quantitative relationships between different morphometric parameters. However, the database lacks sufficient numbers of study cases in mixed carbonate-siliciclastic margins.

Along the Great Barrier Reef (GBR) margin of north-eastern Australia - the largest extant mixed carbonate-siliciclastic province in the world - research on deep-water settings has mainly focused on hemipelagic sedimentation, submarine canyons, sediment gravity flow deposition, and palaeoclimatology (Alexander et al., 1993; Glenn et al., 1993; Dunbar et al., 2000; Dunbar and Dickens, 2003a,b; Kershaw et al., 2003; Page et al., 2003; Lawrence and Herbert, 2005; Puga-Bernabéu et al., 2011, 2013b, 2014; Webster et al., 2012). Studies on mass-wasting processes on the GBR have received considerably less attention (Watts et al., 1993), and the only studies that have dealt in detail with past submarine landslides and potential slope failures come from a few locations (Puga-Bernabéu et al., 2013a, 2017, 2020; Webster et al., 2016). This paper presents the first comprehensive inventory of submarine slope failures along this archetypal margin. We have used the most

comprehensive bathymetric datasets available for this ~500 km long section of the margin to map the distribution of the submarine landslides and analyse their morphometric characteristics. The objectives of this work are to provide an overview of the sedimentary processes, their implications for better understanding failure mechanisms on this margin, and to examine their similarities with other counterparts in different tectonic settings.

2. Regional setting

2.1. Geological setting

The north-eastern Australia margin is a passive continental margin that constitutes an excellent analogue for carbonate and mixed carbonate-siliciclastic sedimentation (Fig. 1A). The gross architecture of this margin is controlled by the rift phase of margin development during the Late Cretaceous–Paleocene-earliest Eocene (Taylor and Falvey, 1977; Gaina et al., 1999; Hill and Hall, 2003). The geologic evolution of north-eastern Australia during the Cenozoic resulted from the interplay of long-term (plate motion and subsidence) and short-term factors (eustasy, climate, oceanography). This evolution has been summarized by Symonds et al. (1983), Davies (2011) and Davies et al. (1989, 1991) and includes five main phases: 1) Clastic fluvio-deltaic and temperate-water carbonate sedimentation during the Eocene and Oligocene; 2) Major marine transgression with development of coralline algal bioherms on the outer shelf and marginal fan deltas during the late Oligocene and early Miocene; 3) Major progradation of the shelf during a falling sea-level period from the middle to the late Miocene, with
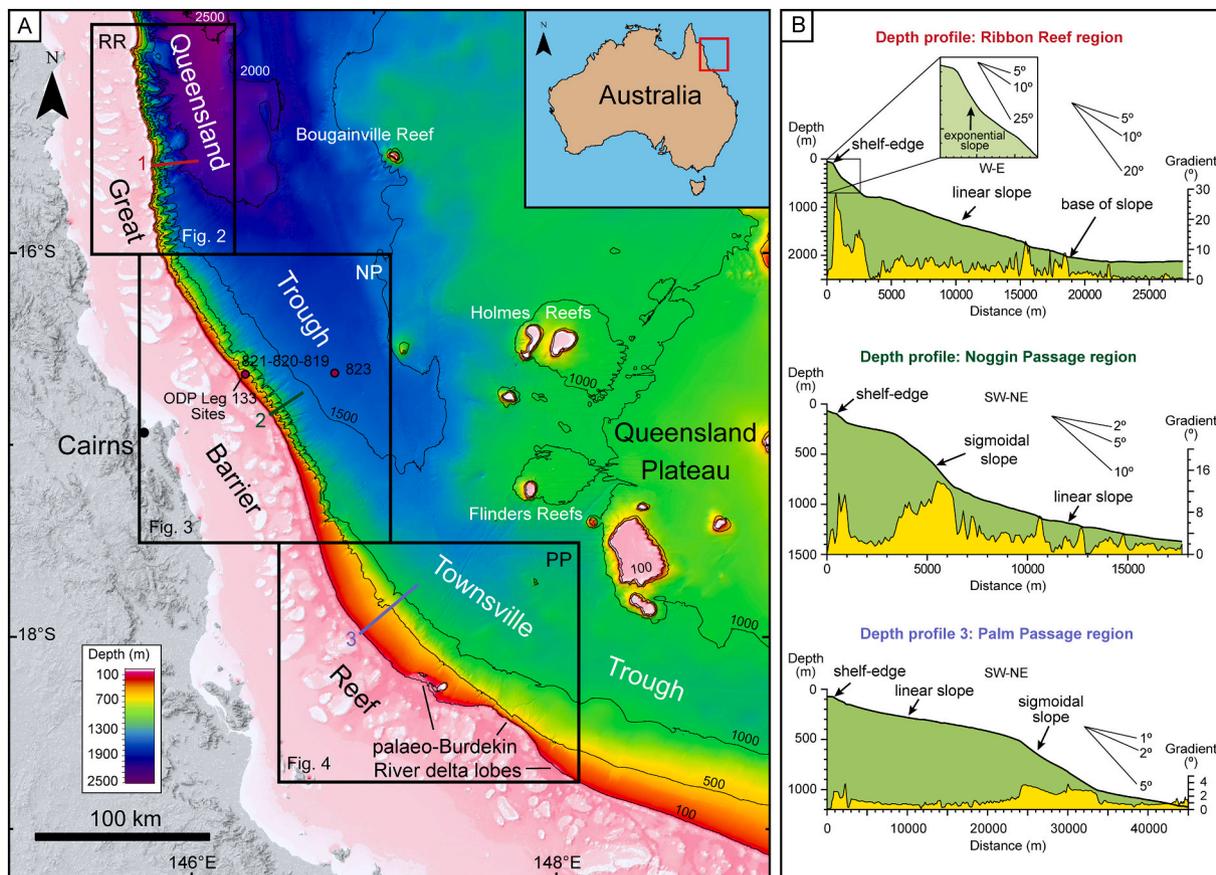

Fig. 1. (A) Bathymetry (100 m resolution DEM) of the north-eastern Australian margin showing the main physiographic regions: The Great Barrier Reef, Queensland and Townsville troughs, and Queensland Plateau. Insets show the location of the study regions. Colour lines and numbers correspond to depth profiles shown in B). Location of Ocean Drilling Program (ODP) Leg 133 Sites 819, 820, 821 and 823 and palaeo-Burdekin River delta lobes are also marked. Study regions RR: Ribbon Reef; NP: Noggin Passage; PP: Palm Passage. Bathymetric contours are given in metres. B) Representative depth profiles across the study regions. Location shown in A). Note the distinctive morphology of the slope along the three regions.

dominant fluvio-deltaic sedimentation and progressively restricted tropical reef growth; 4) Uniform subsidence of the shelf during the Pliocene balanced by shelf aggradation, with alluvial sedimentation during low sea-level and prograding fluvio-deltaic sediments deposited during high sea-level; 5) A reef-building phase during the Pleistocene with widespread reef growth since 500–700 ka (Webster and Davies, 2003; Braithwaite et al., 2004; Dubois et al., 2008; Humblet and Webster, 2017).

Modern surface sediments on the slope and basin comprise both siliciclastics and biogenic carbonates (Dunbar et al., 2000; Francis et al., 2007). Available subsurface data on the slope from long Ocean Drilling Program (ODP) cores (Leg 133, Sites 819, 820 and 821) (Fig. 1) record a Pleistocene-Holocene (<1.5 Ma) mixed carbonate–siliciclastic sedimentary succession at least 400 m thick (Davies et al., 1991). This succession includes cyclic bundles of coarsening- and fining-upward clay-rich and carbonate-rich oozes (Glenn et al., 1993). Abundant sediment gravity flow and mass-transport deposition have been recorded on the basin floor since the middle Miocene (phase 3). Renewed faulting, subsidence, and associated tectonic tilting were likely the main factors favouring shelf and slope sediment redeposition during the Miocene and early Pliocene, while relative sea-level fluctuations and margin morphology played an important role during the Pleistocene (Watts et al., 1993; Puga-Bernabéu et al., 2014). Average sedimentation rates on the slope were relatively high (30–40 cm/ky) during the middle Pleistocene and decreased to 8–11 cm/ky during the late Pleistocene (Davies et al., 1991). Studies on piston cores revealed that sedimentation rates on the slope were one order of magnitude higher during the transgression and sea-level highstands (22–55 cm/ky) than during sea-level lowstands (2–6 cm/ky) (Dunbar et al., 2000).

2.2. Margin morphology

We focused our investigation on submarine landslides on the northeastern Australia margin between latitudes 14°45′S and 18°45′S along a distance of ~500 km. This part of the margin can be divided into three regions characterized by different outer shelf and slope morphologies, named from north to south: Ribbon Reef (RR), Noggin Passage (NP) and Palm Passage (PP) (Fig. 1A) (Puga-Bernabéu et al., 2013b, 2014). The shelf edge deepens from RR (~70 m water depth) to NP and PP (~105 m) (Abbey et al., 2011), and the extensive shelf-edge barrier system in the RR region changes to more open conditions without near-continuous reef barriers in NP and PP. The slope morphology shows a significant latitudinal variation (Puga-Bernabéu et al., 2013b) (Fig. 1B). In the RR region, the continental slope extends down from the shelf edge to a depth of 2250 m across a horizontal distance of 10 to 30 km, with average gradients of >6°. The depth profile across the slope is linear to exponential, with a very steep uppermost part (average gradient of 25°) changing to moderately steep (5° to 10°) below ~300 m (Fig. 1B). The steep slope in the RR region is shaped by large, mostly shelf-incised submarine canyons. In the NP region, the slope exhibits sigmoidal depth profiles from the middle slope and linear profiles from the lower slope. It extends from the shelf edge down to 1300–1600 m across a horizontal distance of 15 to 20 km (Fig. 1B). The slope is moderately steep (~4°), showing the steepest gradients (~15°) in the middle slope, generally between 400 and 800 m, and is incised mainly by slope-confined canyons. In the PP region, the slope widens up to ~40 km across with an average gradient of <2°. This slope exhibits a gently sigmoidal depth profile on the middle slope and is not dissected by well-developed submarine canyons (Fig. 1A, B). The continental slope passes laterally to the basin floor of the narrow structural depression of the Queensland and Townsville troughs (Fig. 1) that gently deepens towards the north, with gradients ranging from ~0.13° in the PP region to ~0.31° in the RR region.

3. Methods, dataset and terminology

3.1. Data and analysis

The submarine landslides were mapped using the multibeam bathymetry data mainly collected during the RV *Southern Surveyor* voyage in September–October 2007 (SS07/2007) and the RV *Southern Surveyor* voyage in 2008 (SS09/2008), using a Kongsberg EM300 multibeam echosounder (30 kHz) (Webster et al., 2008; Tilbrook and Matear, 2009), and later compiled with all available bathymetry data for the study area to produce a 30 m Digital Elevation Model (DEM) (Beaman, 2018). The resulting bathymetry data were incorporated into ESRI ArcGIS 10.5 and QPS Fledermaus 7.8, and provide the basis for the morphometric analysis of the submarine landslides. The morphometric analysis also included the calculation of slope gradient using the ArcGIS Spatial Analyst tool to improve the identification of the landslides by highlighting the steep slopes of the headscarps.

This inventory includes submarine landslides originating on the slope (not in submarine canyons) that cover an area of >1 km². Multiple perspective views of the bathymetric DEM and derived slope gradient maps (Figs. 2, 3 and 4), and depth cross-section profiles were examined to evaluate the existence of clear headscarps and sidewalls that form part of a mappable landslide scar. Once outlined, the dimensions of the failures and additional morphometric parameters were measured and compiled (Fig. 5). Landslide volume was calculated by comparing pre-landslide and post-landslide bathymetries following the approach of ten Brink et al. (2006) and Völker (2010): 1) digitalizing the detailed polygon that encompasses each landslide; 2) interpolating and gridding the polygon surfaces to obtain a pre-failure surface; and 3) subtracting the interpolated surfaces from the present-day topography to obtain the volume loss in each failure. The runout distance has been conservatively measured as the landslide length when no obvious failed sediment is observed in the distal part of the landslide.

The information of each landslide is not fully uniform or shows the same quality through the entire database because the outlines of some failures were difficult to evaluate, especially at the downslope end where the toe is locally obscured in the bathymetry data. In such cases, we provide a conservative measurement (e.g., total length) or the parameter is not compiled for that feature (e.g., gradient of adjacent slope). The type of landslide intrinsically precludes in many cases the measurement of some of the dimensions and morphometric parameters (e.g., slope gradient at origin in landslide complexes, see Section 3.3). As in other submarine landslide inventories (e.g., McAdoo et al., 2000; Alberico et al., 2018), the dataset might be biased towards the more recent events and/or towards the largest events due to the coalescence of multiple small events that might be unrecognizable with time as we used only seabed surface data.

3.2. Correlation between morphometric parameters

Spearman's rho (ρ) rank correlation coefficient was calculated for all morphometric parameters and ratios measured in the different landslide types in order to reveal the possible relationships between them (McAdoo et al., 2000; Hühnerbach et al., 2004; Moernaut and De Batist, 2011; Casalbore et al., 2020). This is a non-parametric coefficient that does not require any specific frequency distribution of the variables, in contrast to the parametric Pearson correlation coefficient that does require a linear relationship. The ρ coefficient indicates whether two parameters vary together, although such parameters are not necessarily dependent on each other. In this study, we consider a high correlation between two parameters when $\rho > 0.7$ and < -0.7, and a moderate correlation when $\rho = 0.5–0.7$ and $-0.5–(-0.7)$. The correlation among the different parameters has been further investigated using scatter plots and the coefficient of determination (R^2) value was used to typify the goodness of the fit of a regression line to the data values.
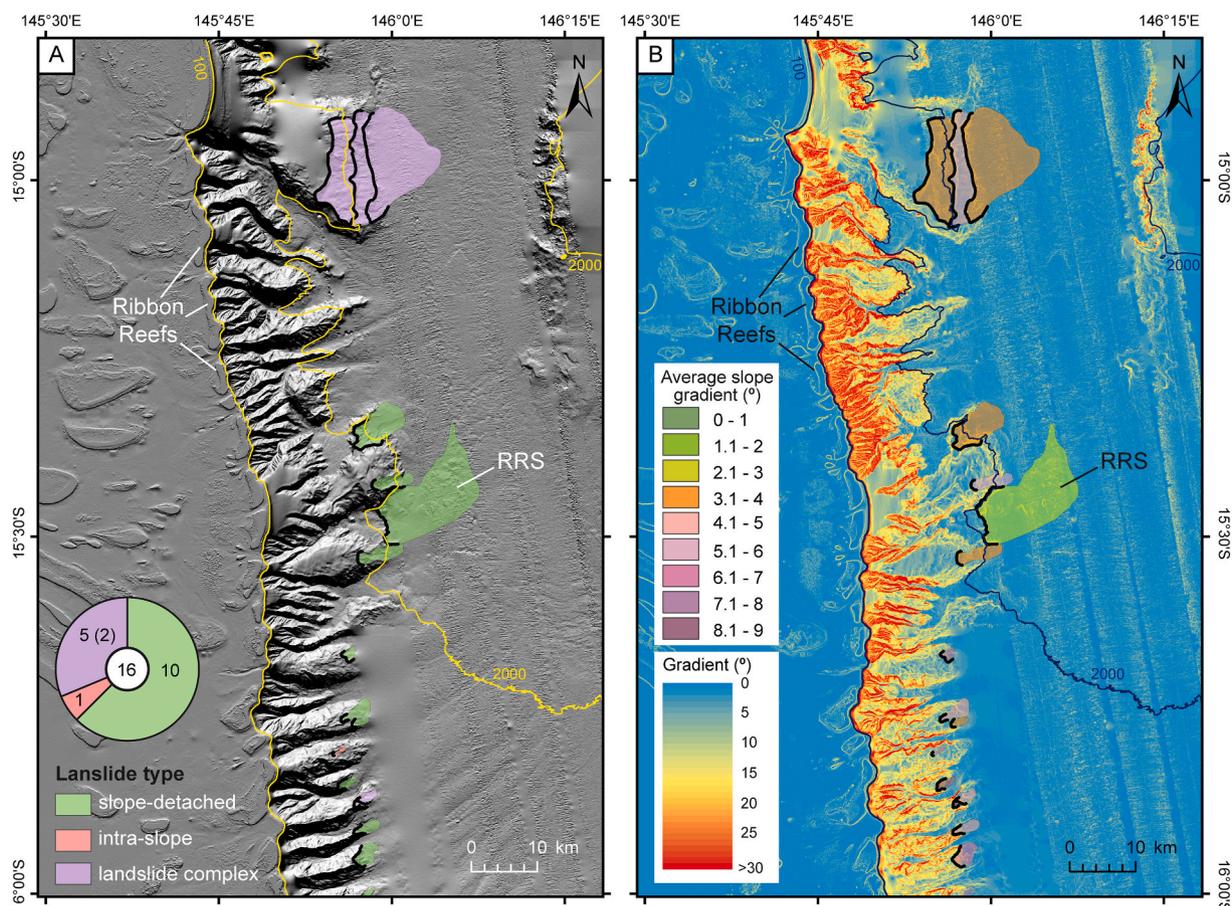
Fig. 2. (A) Submarine landslide distribution on the Ribbon Reef region (see Fig. 1 for location) revealed by available multibeam bathymetry (hillshaded 30 m resolution DEM; Beaman, 2018). Individual landslides within landslides complexes are also delineated. Pie chart shows the number of landslides by type. In the landslide complex type, the number corresponds to the individual landslides within landslide complexes, which are given in brackets. RRS (Ribbon Reef Slide) is the representative slope failure of this region (Puga-Bernabéu et al., 2020). Bathymetric contours (yellow lines) are given in metres. (B) Landslide distribution as in A) on the gradient map derived from the DEM. Each landslide takes the colour of the average slope gradient that existed before the slope failure. Bathymetric contours (blue lines) are given in metres.

3.3. Magnitude-frequency statistical analysis

Frequency-size distribution plots quantify the number of events of various sizes in a given region, and in the case of submarine landslides, it mostly conforms to negative power law-like distribution (power law hereafter) (Micallef et al., 2008), and in fewer cases, to lognormal (Chaytor et al., 2009) or logarithmic (Issler et al., 2005) distributions. However, these modelled distributions may be approximated only for a certain range of the event frequency distribution dataset. Consequently, the resulting distribution model describes only a biased part of the data as these data alone are not robust enough to be characterized as the definitive model (Clauset et al., 2009). Additionally, power-law fitting with methods, such as least squares introduces further systematic biases and inaccuracies to the power-law parameters (Clauset et al., 2009). In this study, we have followed the method detailed in Clauset et al. (2009) using the poweRlaw package (Gillespie, 2015a,b) for R software (R Development Core Team, 2020).

Previous authors have attempted to fit landslide empirical volume data to power-law cumulative probability distribution functions (Casas et al., 2016), as well as to relate them with the number of events distribution (Urgeles and Camerlenghi, 2013). Power-law cumulative probability distribution functions p(x) are mathematically determined by the following equation:

$$p(x) \propto x^{\alpha} \text{ for } x \geq xmin$$

where α is a scaling exponent and x is the variable of interest (Clauset et al., 2009). To calculate α, the lower bound of the power law (x-min) must be estimated beforehand, since the tail of the distribution is where the large fluctuations of values that define a possible power-law distribution are located. Estimating the lower bound could be made visually using a log-log plot; however, this is a subjective approach depending on the observer. Erroneously estimating a lower threshold will not offer a good power-law fit. Similarly, a high threshold will lower the number of samples in the fitting, leading to an error-prone method. Instead, x-min and α have been calculated using the poweRlaw package (Gillespie, 2015a,b) for R (R Development Core Team, 2020) which implements the method described in Clauset et al. (2009). The lower bound of the tail is calculated and tested with a goodness of fit via bootstrapping. This goodness of fit was calculated with the Kolmogorov-Smirnov statistic p-test. When the *p*-value is >0.05–1, the hypothesis cannot be rejected, and it is acceptable to assume that the dataset is statistically sampled from a power-law distribution. The exponent of the power law (α) is calculated by maximum likelihood estimation. However, although *p*-values > 0.1 indicate that the empirical data are similar to a synthetic power-law cumulative distribution, it does not determine if other distributions (e.g., lognormal or exponential) should be rejected. For this reason, a comparison between distributions was performed via maximum likelihood estimation (MLE) using the R package poweRlaw (Gillespie, 2015a,b), which follows the method described by Clauset et al. (2009). When the result of the MLE hypothesis is close to zero, both distributions are considered to be equally far from the true distribution,
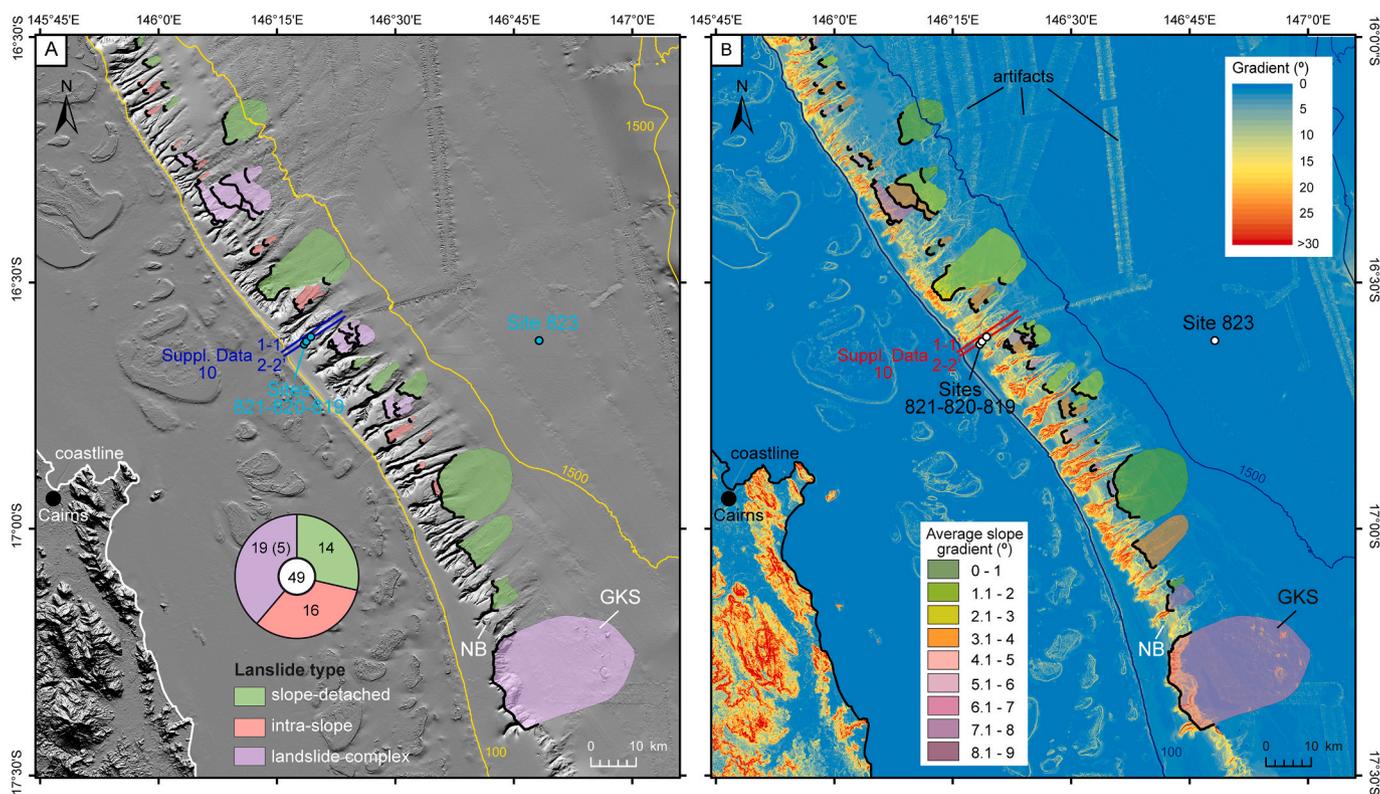
Fig. 3. (A) Submarine landslide distribution on the Noggin Passage region (see Fig. 1 for location) revealed by available multibeam bathymetry (hillshaded 30 m resolution DEM; Beaman, 2018). Individual landslides within landslides complexes are also delineated. Pie chart shows the number of landslides by type. In the landslide complex type, the number corresponds to the individual landslides within landslide complexes, which are given in brackets. GKS (Gloria Knolls Slide) is the representative slope failure of this region (Puga-Bernabéu et al., 2017, 2020). NB (Noggin Block) is a portion of the upper slope that may potentially fail under certain seismic conditions (Puga-Bernabéu et al., 2013a). The location of the Ocean Drilling Program Leg 133 Sites 819, 820, 821 and 823 and depth profiles shown in Supplementary data 10 are also indicated. Bathymetric contours (yellow lines) are given in metres. (B) Landslide distribution as in A) on the gradient map derived from the DEM. Each landslide takes the colour of the average slope gradient that existed before the slope failure. Bathymetric contours (blue lines) are given in metres.
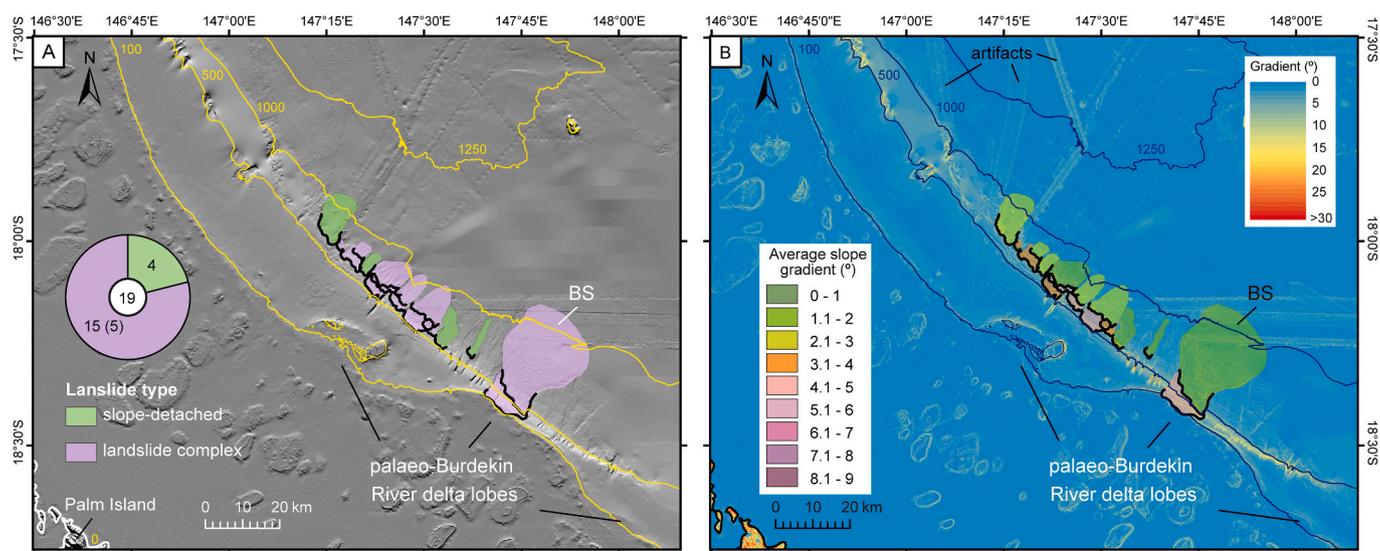

Fig. 4. (A) Submarine landslide distribution on the Palm Passage region (see Fig. 1 for location) revealed by available multibeam bathymetry (hillshaded 30 m resolution DEM; Beaman, 2018). Individual landslides within landslides complexes are also delineated. Pie chart shows the number of landslides by type. In the landslide complex type, the number corresponds to the individual landslides within landslide complexes, which are given in brackets. BS (Bowl Slide) is the representative slope failure of this region (Puga-Bernabéu et al., 2020). The location of the palaeo-Burdekin River delta lobes is also indicated. Bathymetric contours (yellow lines) are given in metres. (B) Landslide distribution as in A) on the gradient map derived from the DEM. Each landslide takes the colour of the average slope gradient that existed before the slope failure. Bathymetric contours (blue lines) are given in metres.
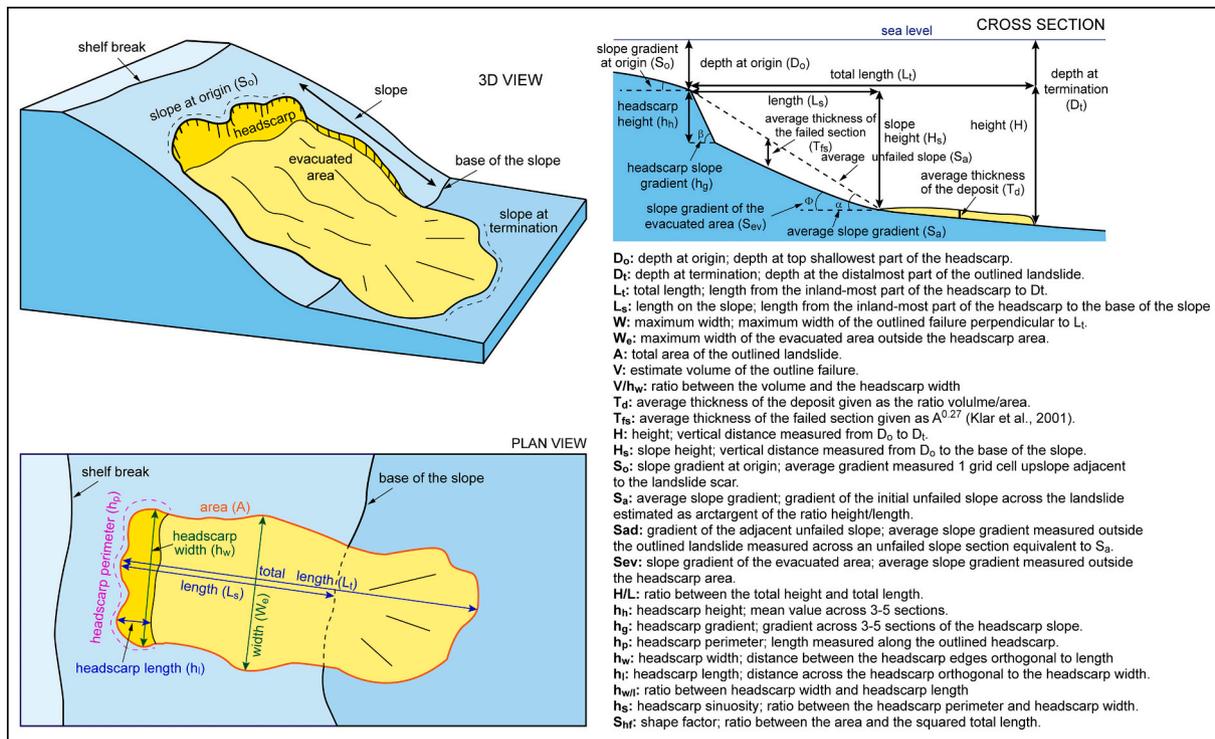
Fig. 5. Sketches showing the morphometric parameters and ratios measured in the submarine landslides on the GBR margin. Definitions of each parameter are also shown.

and it is not possible to discriminate between them. Positive results far from zero could favour the power law model over the alternative, and vice versa, the negative results favour the alternative model. To fully differentiate them, a p-test over one-side or two-sides may be applied. The one-side p-test aims to assess the hypothesis of the power law being a better model over the alternative, whereas a two-side p-test does not consider the order of the comparison. In our analysis, the empirical data fitted to a power-law distribution were compared with lognormal and exponential distributions. While it was noted by Clauset et al. (2009) that the minimum number of observations in the lower tail should be larger than 100, our data are limited by its nature, yet previous authors have fitted power-law distributions to less than 100 of observations (Urgeles and Camerlenghi, 2013; Moernaut and De Batist, 2011).

The empirical data, calculated by applying a cut-off value at the lower tail of the distribution, were fitted to a power-law function calculated by nonlinear least squares (NLS) using R software. This function relates the number of events (NL) versus volume (V) distribution ($N_L = aV^\theta$), where a is a multiplier and θ a scaling exponent. We also fitted the empirical data to power-law, logarithmic and exponential functions using regression lines by the least squares method, to enable comparison with datasets from other regions that have used such an approach.

Additionally, we fitted the landslide frequency-size of volume, area and length to a lognormal distribution for comparison with other data-sets. The probability density function for the lognormal distribution of landslides dimensions f(x) is given by:

$$f(x) = \frac{1}{\sigma x \sqrt{2\pi}} e^{\frac{-(ln(x)-\mu)^2}{2\sigma^2}} \tag{1}$$

where σ is the shape parameter (or ln standard deviation) and μ is the location parameter of the curve (or ln mean). The corresponding cumulative distribution function is given by:

$$F(x) = \frac{1}{2} erfc\left(\frac{\ln x - \mu}{\sigma\sqrt{2}}\right) \tag{2}$$

where erfc is the complementary error function. Once we obtained the σ and μ parameters, we performed 10,000 Monte-Carlo simulations and used the average of the simulated curves for comparison against our dataset. The coefficient of determination was obtained as the mean of the coefficients obtained from the correlation of our dataset with 100 simulations. We performed the lognormal fitting only to datasets with more than 50 landslides to avoid bias as suggested by Geist and ten Brink (2019).

In this work, we have studied the cumulative frequency-size distribution of the GBR margin landslides. Other studies have quantified the occurrence of landslides using non-cumulative frequency distributions (Micallef et al., 2008), especially when the tail of the probability distribution is a power law. We note that both distributions can be related, taking into account that the scaling exponent for the power law (θ) in the cumulative frequency distribution can be related with the scaling exponent (β) in the non-cumulative frequency distribution as $\beta = \theta + 1$ (Malamud et al., 2004).

3.4. Terminology

In this study, we use the general terms 'landslide' or 'slope failure', as determining the typology of these features (i.e., whether slides, slumps or debris flows) based solely upon bathymetry data alone is very difficult. Submarine landslides along the north-eastern Australia margin fall into two categories according to their source: those that are sourced in submarine canyons, and those that originated on the open slope between canyons. This study is only focused on landslides that occur on the open slope between canyons. Open slope landslides are here grouped into two sub-groups: those that remove slope material and extend downslope beyond the continental rise (herein slope-detached landslides), and those that erode the slope without extending to the basin floor (herein intra-slope slides). The term landslide complex is used here to name two or more adjacent slide scars with headwall scarps arranged in a staircase pattern. The landslides that form a landslide complex are herein referred to as individual landslides within a complex.

4. Results

4.1. Morphology, type and distribution of the landslides

A total of 84 open slope submarine landslides were mapped along a ~500 km long section of the margin, between 14.45°S and 18.75°S latitude (Figs. 2, 3 and 4), which represents the most comprehensive inventory of slope failures on the Australia margin. They are grouped into 28 slope-detached landslides, 17 intra-slope landslides and 12 landslide complexes comprising 39 landslides. The mapped landslides cover an area of ~2940 km^2 in the slope and basin, and have eroded a volume of ~73 km^3 from an area of ~1605 km^2 (~12.6%) of slope (Table 1). The area removed from the slope is similar to the slope area excavated by submarine canyons along the study area (~1700 km^2) (Table 1). The number and extent of the slope failures vary between the different physiographic regions (Figs. 2, 3 and 4; Table 1), being more abundant and extending over a larger area in the NP region (i.e., 49 landslides, 1.3 landslides/100 km^2 of slope).

The landslides fall within the translational type according to the Skempton ratio (0.004–0.09) (approached as the maximum headscarp height to landslide length ratio; ratios of <0.15 define translational landslides; Skempton and Hutchinson, 1969), although landslide complexes cannot be categorized within this type only from the bathymetry. The smaller sized (<10 km^2) landslides have relatively elongated morphologies in plan-view with the shape factor commonly <0.57, while circular shapes are more abundant in larger landslides and landslide complexes. Failed sediment has presumably been evacuated from the scar areas to deeper waters in most of the landslides as no debris or blocks remained close to the landslide headscarp (disintegrative sensu McAdoo et al., 2000) except for a few cases (Puga-Bernabéu et al., 2020). Alternatively, they might have been buried by younger sediments or eroded by subsequent sediment gravity flows (Puga-Bernabéu et al., 2017).

4.2. Landslide morphometric characteristics

This section provides detailed information on the main morphometric characteristics measured in the different types of landslides and their descriptive statistics, as well as their spatial distribution along the margin. A summary of the measurements is shown in Fig. 6, Table 2 and the Supplementary data 1 and 2.

4.2.1. Slope-detached landslides

Slope-detached landslides originate mostly on the middle and lower slope in water depths between ~490 m and ~1920 m. They extend down to water depths between ~950 m and ~2275 m onto the basin floor, with a mean height of 370 m and a median slope height of 333 m. Slope-detached landslides occurred on average slope gradients of 3.7° ±

Table 1

Summary of the distribution of the submarine landslides on the Great Barrier Reef (GBR) margin.

	RR	NP	PP	GBR
N° landslides	16	49	19	84
Total margin area[a] (km^2)	4046	9314	5634	18,994
Total landslide area (km^2)	470	1496	972	2938
Slope area (km^2)	3899	3792	5070	12,761
Failed area on the slope (km^2)	252	728	626	1606
% failed area on the margin	11.6	16.1	17.3	15.5
% failed area on the slope	6.5	19.2	12.3	12.6
N° landslides/100 km^2	0.41	1.29	0.37	0.66
Slope volume mobilized (km^3)	6.9	52.8	12.9	72.6
Area covered by canyons (km^2)	752	698	247	1696

RR: Ribbon Reef; NP: Noggin Passage; PP: Palm Passage.

[a] Area measured from the shelf break to the axis of the Queensland and Townsville troughs (see Fig. 1 for locations).

1.8 (median = 3°). Their slope gradient at origin is 5.8° ± 2.5 (median = 4.7°) and their adjacent unfailed slope is 3.9 ± 2.3 (median = 3°). Length and width of the evacuated area range one order of magnitude, with median values of ~6800 m and ~2730 m, respectively. Most slope-detached landslides cover areas of <50 km^2 and have remobilized volumes of <1 km^3, with only a few cases affecting areas that exceed 100 km^2 and involve volumes of up to 7.8 km^3. The landslide scars have arcuate shapes (mean width/length ratios of 2.2), with widths between 950 m and 13,960 m. The headscarp perimeter length ranges from about 1720 m to 20,040 m, yielding a mean sinuosity index of 1.86. The headscarp height ranges from ~20 m to ~385 m and their gradient is always steeper than the adjacent unfailed slope, generally over 8°. The estimated thickness of the failed section is between 52 m and 180 m, and the average thickness of the deposit has a mean value of 15.4 m.

4.2.2. Intra-slope landslides

Intra-slope landslides originate mostly on the middle slope, and to a lesser extent, on the lower slope in depths between ~570 m and 1185 m, extending down to 880–1415 m, with a mean height of ~264 m. These intra-slope landslides are overall smaller than their slope-detached counterparts. The median intra-slope landslide is ~3580 m long and ~1260 m maximum width, covering an area of 3.6 km^2. The median volume of sediment mobilized is 0.033 km^3 and has an average thickness of about 7.5 m. The average pre-failure slope gradient was 4.1° ± 1.1 (median = 4°) with the landslides originated at slopes gradients of 6.8° ± 2.3 (median = 7.5°). Landslides scars have curved shapes (mean width/length ratios of 2.2), with a mean length of ~660 m and a perimeter length from ~745 m to ~5440 m along the slope that yields a mean sinuosity index of 1.81. The headscarps have a mean slope gradient of 11.1° and their height seldom exceeds 100 m.

4.2.3. Landslide complexes

The landslide complexes comprise two to seven juxtaposed landslides forming seafloor features that likely resulted from retrogressive failure, although independent failure events cannot be discounted. The shallowest part of these landslides lies across the entire slope depths ~100–1680 m, where the mean gradient of the unfailed slope covered by the landslide complex is 3.6° ± 1.0 (median = 3.3°) and extends down to ~940–2450 m. The median individual landslide forming the complexes is ~4115 m long and ~3615 m wide, and covers an area of 9.6 km^2. Landslide complexes have median values of about 12.7 km long and 7.4 km of maximum width, extending over ~70 km^2 on the seafloor, and have remobilized 1.04 km^3 of sediment, although the value of these dimensional parameters can vary up to three orders of magnitude (Table 2). The height of the headscarps of individual landslides within the complexes ranges from 25 m to 214 m (670–830 m in the Gloria Knolls Slide, Puga-Bernabéu et al., 2017), with mean headscarp slope gradients of 9.0°. The morphology of the scars is widely variable, from semicircular to cauliflower-shape or linear (mean width/length ratios between 0.8 and 9.9), either for individual landslides within the complex or composite headscarps in the full landslide complex.

4.2.4. Distribution of morphometric parameters by landslide type

Slope-detached landslides, intra-slope landslides and landslide complexes share some characteristics but they differ in a variety of aspects (Fig. 7; Supplementary data 3). Intra-slope landslides are smaller and landslide complexes are the largest by an order of magnitude. The area of the intra-slope landslides is within a narrow range (1–12 km^2), while slope-detached and landslide complexes exhibit a wider range, skewed to smaller areas of <10 km^2 in the former and to larger (>50 km^2) areas in the latter (Fig. 7-2). Landslide volume, the width of the evacuated area and total length show similar trends than area, although the total length is more widely distributed in landslide complexes (Fig. 7-1, -3, -4). The estimated thickness of the deposits is skewed to values of <15 m for intra-slope landslides, landslide complexes and individual landslides within complexes, while slope-detached landslides
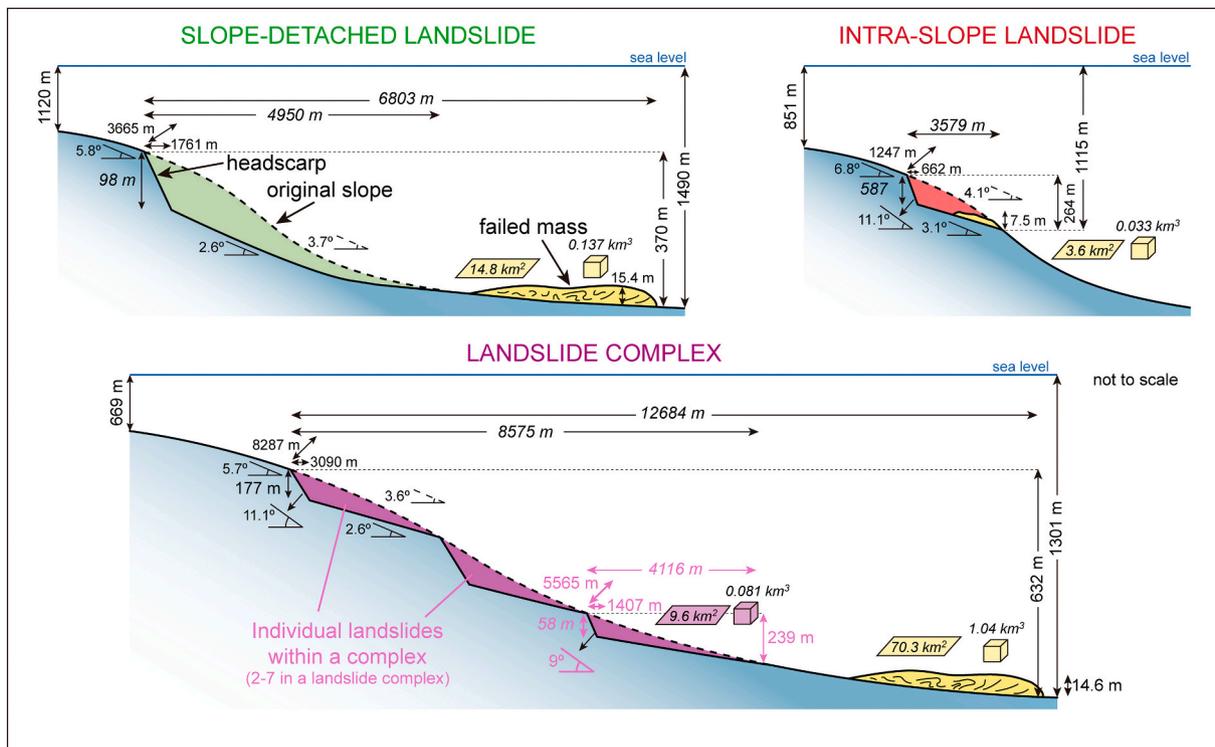
Fig. 6. Sketches showing the different types of submarine landslides on the GBR margin and a summary of their main morphometric parameters. Values correspond to the mean for depth, total height, headscarp width, headscarp length, average thickness and gradients. Median values are given in cursive for the total length, length on the slope, area, volume and headscarp height. Definition of each parameter is given in Fig. 5.

show a wider distribution (Fig. 7-5). Slope-detached failures initiated at depths deeper than the intra-slope landslides and landslide complexes, and accordingly, the depth at their termination is also deeper (Fig. 7-6, -7). Similarly, the gradients of the slope at origin and unfailed slopes are steeper in the intra-slope landslides, and they are similar between slope-detached and landslide complexes (Fig. 7-8, -9). The height drop is higher in the landslide complexes as they comprise several (likely retrogressive) failures, but the height of individual landslides in the complexes is similar to intra-slope landslides (Fig. 7-10). The headscarp perimeter and headscarp width are similar between individual landslides complexes and slope-detached landslides, while intra-slope slides are shorter and narrower (Fig. 7-11, -12). The width/length ratio of intra-slope and slope-detached landslides is within a relatively narrow range (~1–4) compared with the individual landslides within complexes and slightly smaller than the landslide complexes (Fig. 7-13). There is no significant difference in the height of the headscarps among the different landslide types, and the headscarp gradient is slightly steeper in the slope-detached slides (Fig. 7-14). The height/length ratio is higher in intra-slope landslides, and comparable between slope-detached and landslide complexes (Fig. 7-15).

4.2.5. Distribution of morphometric parameters by region

To fully exploit the morphometric analysis and understand the influence of different geomorphological settings, this section summarizes the distribution of the morphometric parameters in the three main physiographic regions (Fig. 8; Supplementary data 2 and 4). The landslide scars are shallower in the PP region (576 m mean depth at origin); landslides in the NP region initiates at a mean water depth of 882 m; and landslides in the RR region are the deepest (1517 m on average) (Fig. 8-1). The depth at termination is consistent with the physiography of the margin, which deepens from the PP to RR region (Figs. 2–4 and 8-2). However, slope-detached landslides and landslides complexes in the PP region have larger height drops (mean ~ 480 m) than in other regions (Supplementary data 2). The largest failures (i.e., volume, area and total

length) are located along the slope of the PP region (Fig. 8-4–7). Landslide area, total length and width of the evacuated area are within a narrow range in the RR and NP regions, and these parameters are more evenly distributed in the PP region (Fig. 8-5–7). The height/length ratio is high (mean 0.081) and distributed over a wider range (0.016–0.152) in RR landslides, while this ratio is low (mean 0.069) in the NP region independent of the landslide type. The lowest height/length ratio corresponds to the landslide complex-dominated PP region (mean 0.049) (Fig. 8-8; Supplementary data 2). The headscarp height and the headscarp gradient are similar in PP and NP regions (median ~ 53–58 m and 9–10°, respectively). The RR region hosts higher and steeper median headscarps (75 m, 11.8°) (Fig. 8-9, -10; Supplementary data 2). The average slope gradient where the landslides were generated is gentler in the PP region (mean 2.8°), followed by that in the NP (mean 3.8°) and RR (4.8°) regions (Fig. 8-11), although the gradient of the unfailed slope behind the scar is within a narrower range in the PP region compared with NP and RR regions (Fig. 8-12). The PP region hosts the widest headscarps but their width/length ratio is similar to NP landslides (mean 3.1 and 3.3 respectively), and both PP and NP regions have slightly larger width/length ratios than in RR landslides (median 2.7) (Fig. 8-13, -14).

4.3. Correlation and dependencies between landslide parameters

There are clear dimensional dependences, such as among landslide total length, headscarp length, width and perimeter, and landslide width with the landslide area ($\rho = 0.86, 0.75, 0.87, 0.86$ and 0.92) and volume ($\rho = 0.78, 0.78, 0.85, 0.85,$ and 0.87). Also, between landslide area and volume ($\rho = 0.93$) and between the height and the volume, area and volume per width unit ($\rho = 0.67, 0.65$ and 0.73) (Table 3). A very good fit to a power-law function was found between the volume and area of the landslides ($R^2 = 0.89$), which is within the common range of $R^2 = 0.7$–0.9 found for submarine landslides elsewhere (Chaytor et al., 2009; Casas et al., 2016; Moscardelli and Wood, 2016) (Fig. 9-1). The scaling

Table 2

Summary of the submarine landslide statistics on the Great Barrier Reef (GBR) margin of north-eastern Australia. Mean, median, geometric mean (g. mean), standard deviation (Std. Dev.), maximum (max.) and minimum (min.) values are given for each parameter (see Fig. 5). Statistics are also given for the dataset considering landslides complexes as a single feature (GBR*) and considering the individual landslides within the landslide complexes (GBR**).

GBR	D_o (m)	D_t (m)	L_t (m)	L_s (m)	W (m)	W_e (m)	A (km^2)	V (km^3)	V/h_w (m^2)	T_d (m)	T_{fs} (m)	H (m)	H_s (m)
Mean	925	1270	6882	6460	5139	5052	43.9	0.932	97,018	11.9	90.9	345	351
Median	878	1184	4448	5260	3071	2929	9.5	0.081	36,391	9.3	76.6	299	347
G. Mean	833	1219	5145	5527	3485	3413	13.3	0.121	39,483	9.1	83.8	301	303
Std. Dev.	396	390	6134	3782	5048	5028	96.6	3.482	201,198	9.1	40.5	195	189
Max.	2181	2450	31,763	19,276	22,364	22,364	576.6	32.000	1,505,685	55.5	232.0	1093	843
Min.	102	605	1000	1236	780	780	1.1	0.002	1660	1.0	42.3	83	112

	S_o (°)	S_a (°)	S_{ad} (°)	S_{ev} (°)	H/L	h_h (m)	h_g (°)	h_p (m)	h_w (m)	h_l (m)	$h_{w/l}$	h_s	Sh_f
Mean	5.7	3.7	3.8	2.7	0.066	95	10.7	7477	4576	1591	3.1	1.73	0.64
Median	4.8	3.6	3.5	2.6	0.064	61	10.0	4008	3014	1028	2.8	1.62	0.46
G. Mean	5.4	3.4	3.5	2.4	0.058	70	10.0	5117	3045	1141	2.7	1.68	0.50
Std. Dev.	2.1	1.6	1.8	1.2	0.032	101	4.1	6950	4396	1529	1.9	0.43	0.55
Max.	11.7	8.6	8.9	6.4	0.152	675	22.1	32,325	21,253	9372	9.9	3.07	3.71
Min.	2.2	1.4	1.8	0.5	0.016	21	4.3	745	497	211	0.8	1.10	0.15

GBR*	D_o (m)	D_t (m)	L_t (m)	L_s (m)	W (m)	W_e (m)	A (km^2)	V (km^3)	V/h_w (m^2)	T_d (m)	T_{fs} (m)	H (m)	H_s (m)
Mean	962	1266	5840	5639	4446	4369	28.5	0.489	73,098	11.5	84.0	303	294
Median	907	1184	4365	4466	2746	2684	7.9	0.078	31,977	9.3	72.9	273	273
G. Mean	886	1214	4578	4868	3107	3044	10.5	0.093	33,725	8.9	78.6	273	259
Std. Dev.	379	387	4578	3307	4324	4296	61.1	1.231	137,047	8.2	33.5	143	150
Max.	2181	2450	27,094	16,419	22,364	22,364	458.1	7.804	998,599	38.2	218.0	748	715
Min.	102	605	1000	1236	780	780	1.1	0.002	1660	1.0	42.3	83	112

	S_o (°)	S_a (°)	S_{ad} (°)	S_{ev} (°)	H/L	h_h (m)	h_g (°)	h_p (m)	h_w (m)	h_l (m)	$h_{w/l}$	h_s	Sh_f
Mean	5.7	3.8	3.9	2.7	0.068	83	10.7	6464	4039	1374	3.1	1.72	0.66
Median	4.8	3.6	3.5	2.7	0.065	61	9.9	3904	2528	931	2.8	1.61	0.45
G. Mean	5.3	3.4	3.5	2.4	0.060	66	9.9	4571	2734	1039	2.6	1.67	0.50
Std. Dev.	2.2	1.6	1.8	1.3	0.032	66	4.2	5769	3884	1160	1.9	0.43	0.59
Max.	11.7	8.6	8.9	6.4	0.152	386	22.1	22,886	17,949	5686	9.9	3.07	3.71
Min.	2.2	1.4	1.8	0.5	0.016	21	4.3	745	497	211	0.8	1.10	0.15

GBR**	D_o (m)	D_t (m)	L_t (m)	L_s (m)	W (m)	W_e (m)	A (km^2)	V (km^3)	V/h_w (m^2)	T_d (m)	T_{fs} (m)	H (m)	H_s (m)
Mean	944	1338	8095	6835	4571	4505	51.5	1.273	129,452	12.9	93.1	394	394
Median	923	1261	5406	6577	2591	2286	9.3	0.081	43,859	9.5	76.1	365	371
G. Mean	857	1295	6144	5987	2994	2937	13.8	0.133	52,263	9.6	84.7	344	354
Std. Dev.	381	369	6754	3664	4937	4930	108.5	4.423	248,343	10.3	44.5	213	183
Max.	1919	2450	31,763	19,276	22,364	22,364	576.6	32.000	1,505,685	55.5	232.0	1093	843
Min.	102	881	1694	1950	780	780	1.1	0.002	3257	1.0	42.3	83	123

	S_o (°)	S_a (°)	S_{ad} (°)	S_{ev} (°)	H/L	h_h (m)	h_g (°)	h_p (m)	h_w (m)	h_l (m)	$h_{w/l}$	h_s	Sh_f
Mean	6.0	3.8	3.9	2.7	0.062	114	11.8	6922	3917	1713	2.5	1.83	0.41
Median	5.5	3.6	3.4	2.7	0.056	66	11.2	3796	2159	1206	2.3	1.70	0.38
G. Mean	5.6	3.5	3.6	2.5	0.056	79	11.0	4486	2525	1159	2.2	1.78	0.37
Std. Dev.	2.3	1.4	1.8	1.2	0.028	124	4.4	7223	4208	1759	1.3	0.46	0.23
Max.	11.3	7.8	8.6	6.3	0.137	675	22.1	32,325	21,253	9372	7.6	3.07	1.71
Min.	2.2	1.5	1.8	1.0	0.016	21	4.8	745	497	211	0.8	1.13	0.15

D_o: depth at origin; D_t: depth at termination; L_t: total length. L_s: length on the slope; W: maximum width; W_e: maximum width of the evacuated area; A: area; V: volume; V/h_w: volume/Headscarp width; T_d: average thickness of the deposit given as V/A; T_{fs}: average thickness of the failed section given as $A^{0.27}$ (Klar et al., 2011); H: total height from D_o to D_t; H_s: height from D_0 to the base of the slope; S_o: slope gradient at origin; S_a: average slope gradient; S_{ad}: slope of the adjacent unfailed slope; S_{ev}: slope of the evacuated area; H/L: ratio total height/total length; h_h: headscarp height; h_g: headscarp slope gradient; h_p: headscarp perimeter; h_w: headscarp width; h_l: headscarp length; $h_{w/l}$: ratio headscarp width/headscarp length; h_s: Headscarp sinuosity; Sh_f: shape factor (A/L_t^2).

exponent of the power function between volume and area is 1.272. There is a moderately good fit to a power function between area and headscarp width ($R^2 = 0.74$) and between volume and headscarp width ($R^2 = 0.73$) (Fig. 9-2, -3), as also shown in the Storegga Slide ($R^2 = 0.7$; Haflidason et al., 2005). Better fits exist between area and volume and the total length (runout) of the different landslide types ($R^2 = 0.88$ and 0.92; Supplementary data 7-2, -7). The released volume per width unit or longitudinal section area (ratio volume/headscarp width) is a parameter used for studying the scaling behaviour of submarine landslides (Issler et al., 2005). In the GBR landslides, this parameter is related to the landslide length ($\rho = 0.81$, $R^2 = 0.72$) (Fig. 9-4). The correlation among all these dimensional parameters is, with a few exceptions,

similar along the different physiographic regions (Supplementary data 6, 7).

Slope failures on the GBR margin are found in all water depths, but the majority (about the half) of the landslides originated at depths between 600 and 1000 m, and about a third between 600 and 800 m (Fig. 10-1). The depth distribution of the landslides is consistent with a lognormal and an inverse Gaussian distribution (Fig. 10-1). In the RR region, the size of the landslides increases with water depth at origin, while the opposite relationship is observed in PP and NP regions (Fig. 10-2). The water depth at origin is positively correlated with the average slope gradient along the margin, but with only a moderate fit ($R^2 = 0.40$–0.46) and without any significant influence on the headscarp
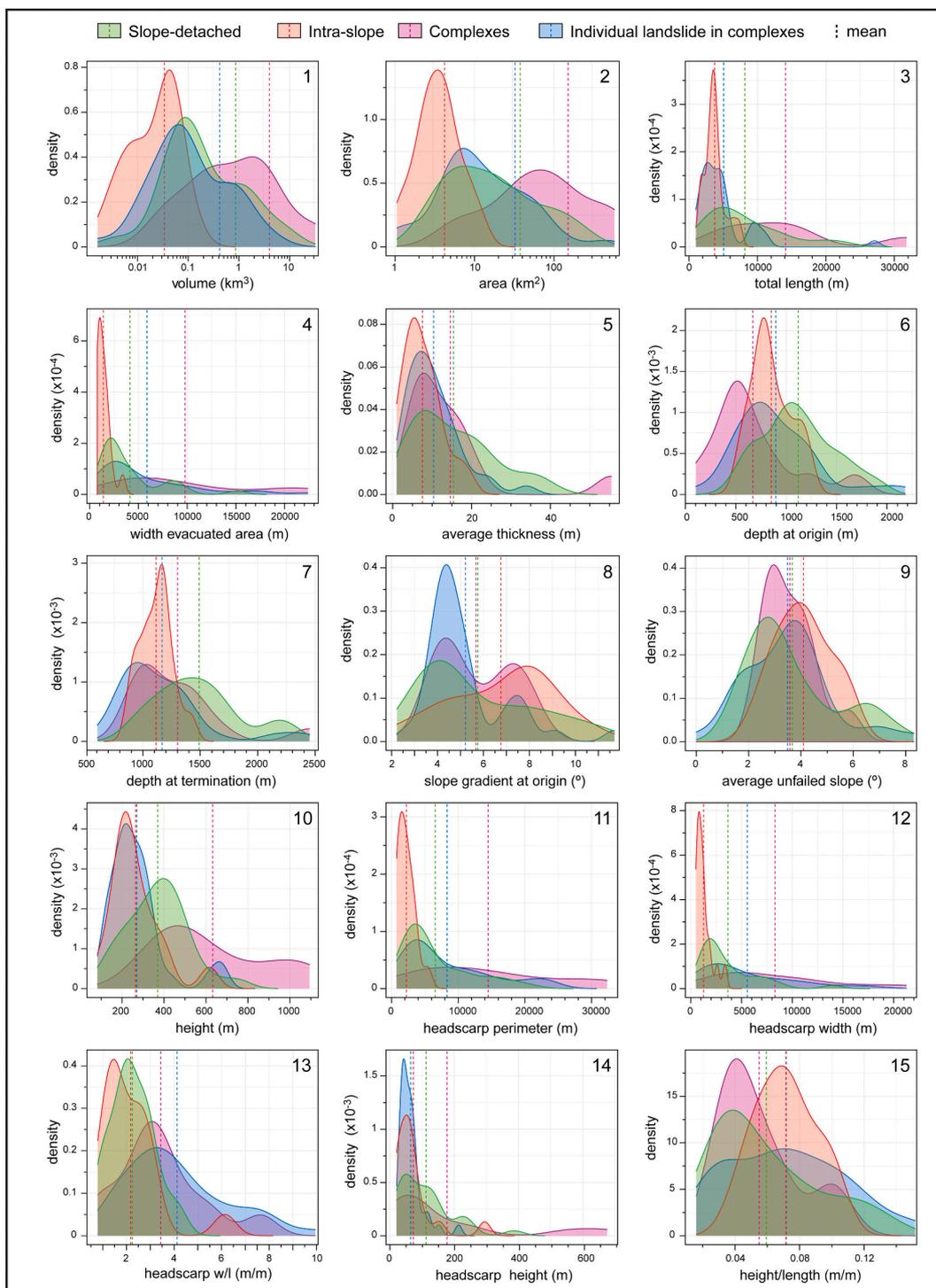
Fig. 7. Density histograms of the morphometric parameters and ratios for different types of submarine landslides on the GBR margin. The vertical axis represents the density of the variable of interest, which is defined as the underlying probability distribution of the data per x-axis unit. Density histograms can be seen as smoothed and continuous histograms where the area below a given curve corresponds to the total number of the variable of interest (e.g., landslide volume data points). Dashed lines mark the mean of the data. Note density histograms for volume (1) and area (2) show a horizontal logarithmic axis.

height (Fig. 10-3). The depth at origin shows strong correlation with the depth at termination ($\rho = 0.82$–89) (Table 3; Supplementary data 6), and a relatively good fit to a linear function ($R^2 = 0.77$) (Fig. 10-4), indicating some bathymetric control on the seafloor extent of the failures across the margin (i.e., the depth at origin somehow conditions the depth where the landslide ends).

The headscarp height may have little effect on the volume of the landslide in the GBR margin as these two parameters are poorly

correlated ($\rho = 0.39$–0.40) and show a very poor fit to any regression function ($R^2 < 0.45$) (Fig. 9-5; Table 3; Supplementary data 6).

On the GBR margin, the headscarp gradient of all the landslides is steeper than the adjacent slope at origin and pre-failed slope (Fig. 9-6, -7). The headscarp gradient does not correlate with the size of the failures ($\rho = 0.06$ and 0.18 for area and volume, respectively) (Table 3). The headscarp gradient shows no obvious relationship with the headscarp height ($\rho = 0.52$), and similarly, the headscarp height is poorly
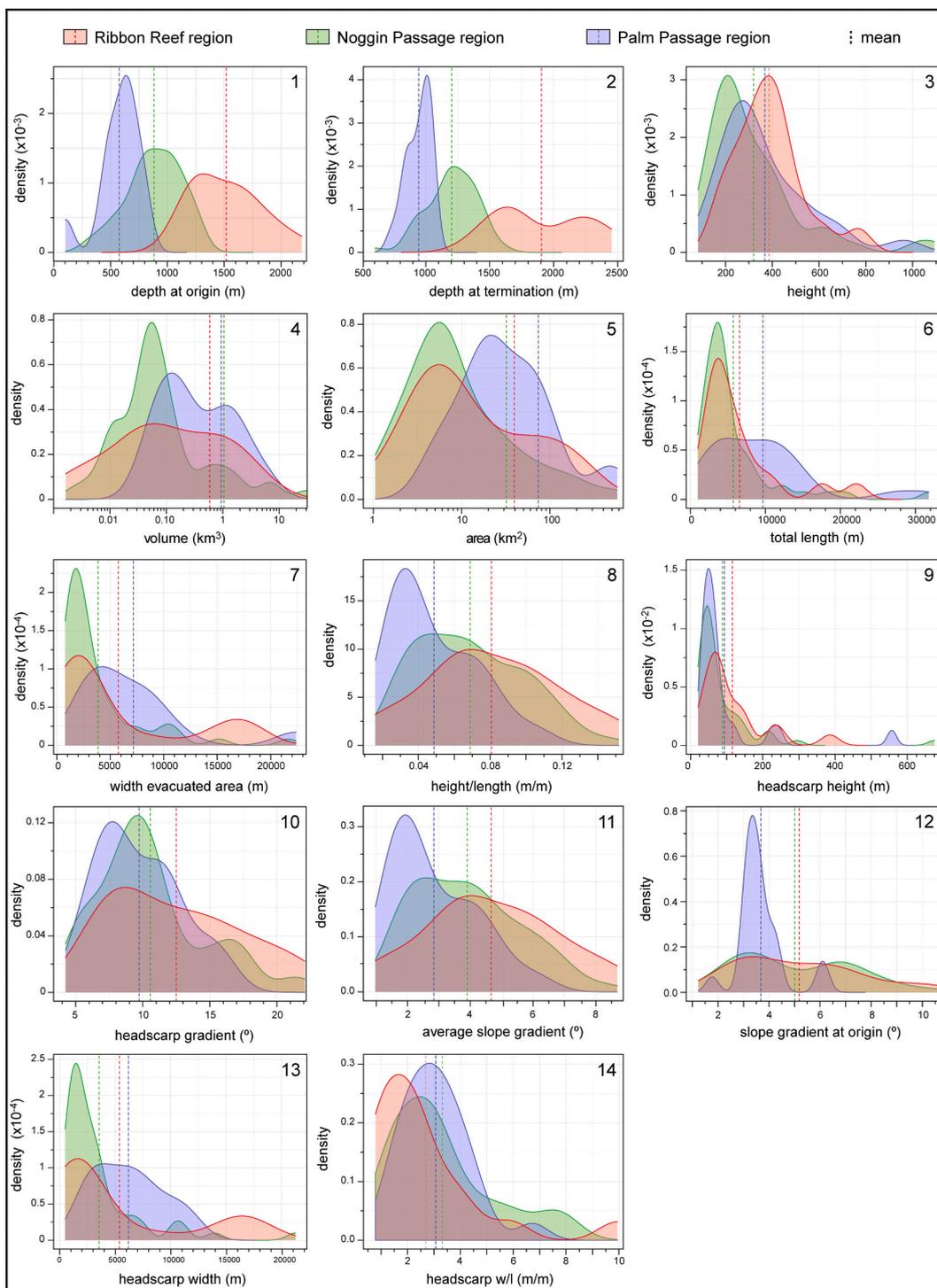
Fig. 8. Density histograms of the main morphometric parameters and ratios for submarine landslides on the different regions of the GBR margin. The vertical axis represents the density of the variable of interest. Dashed lines mark the mean of the data. Density histograms for each region are represented considering the individual landslides within the landslide complexes. For statistics considering landslides complexes as a single feature see Supplementary data 2. Note density histograms for volume (4) and area (5) show a horizontal logarithmic axis.

correlated with the slope gradient ($\rho = 0.38$, 0.27 and 0.20 for the unfailed slope at origin, average unfailed slope and adjacent slope gradient, respectively) (Table 3). This contrasts with the relatively good correlation ($\rho = 0.6$–0.7) found in the U.S. continental margins (McAdoo et al., 2000).

As in other continental margins (e.g., North Atlantic, west U.S. coast; McAdoo et al., 2000; Hühnerbach et al., 2004), the size (area and volume) and total length (i.e., runout) of landslides on the GBR margin

show a very poor or negative correlation with increasing slope gradient ($\rho < -0.27$) (Table 3; Supplementary data 6). In contrast to other continental margins, the largest GBR landslides are not related to gentler slopes at origin. For example, some of the largest landslides and with longest runout distances were originated at slope gradients close to or slightly steeper than the median value (5.7°) for the entire dataset (Supplementary data 5-4). However, among them only the largest landslide in the GBR (the GKS; Puga-Bernabéu et al., 2017) (Fig. 3) was
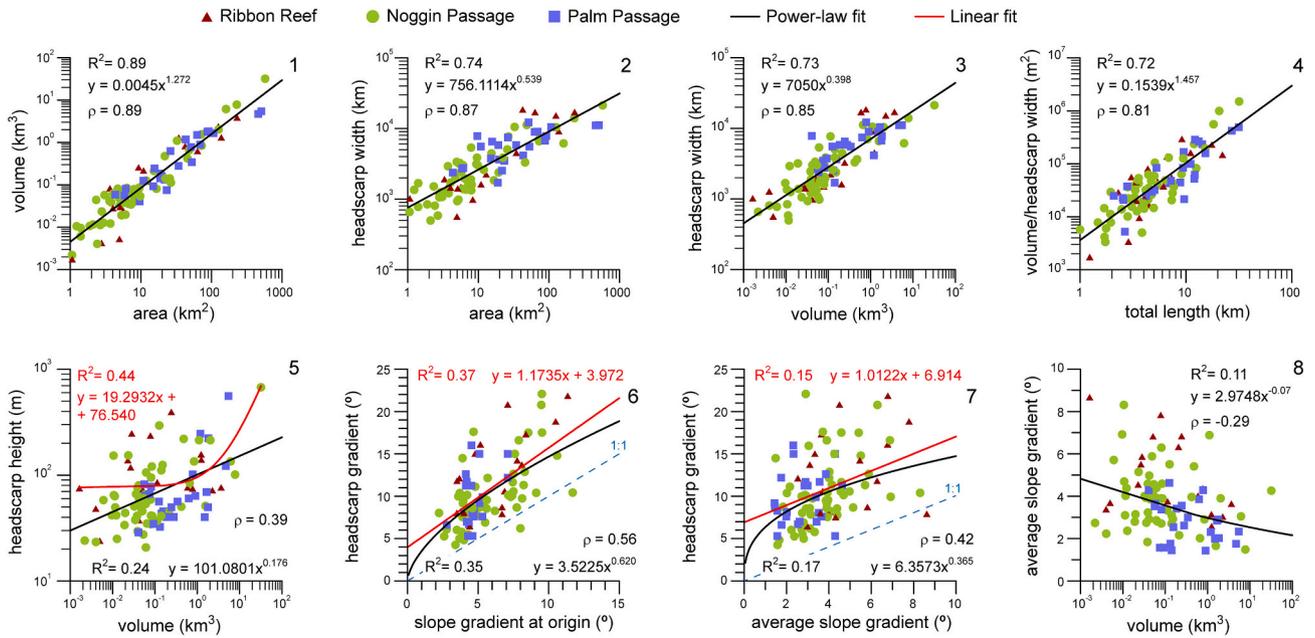
Fig. 9. Scatter plots of selected morphometric parameters and ratios for submarine landslides on the GBR margin. The region of each failure is indicated in the legend. Spearman rank coefficient (ρ) as in Table 3, regression lines and corresponding equation to a power-law and/or linear fit (black and red lines/letters, respectively) and coefficient of determination (R^2) are given for each plot. Dashed blue line in 6 and 7 corresponds to a gradient ratio of 1:1.
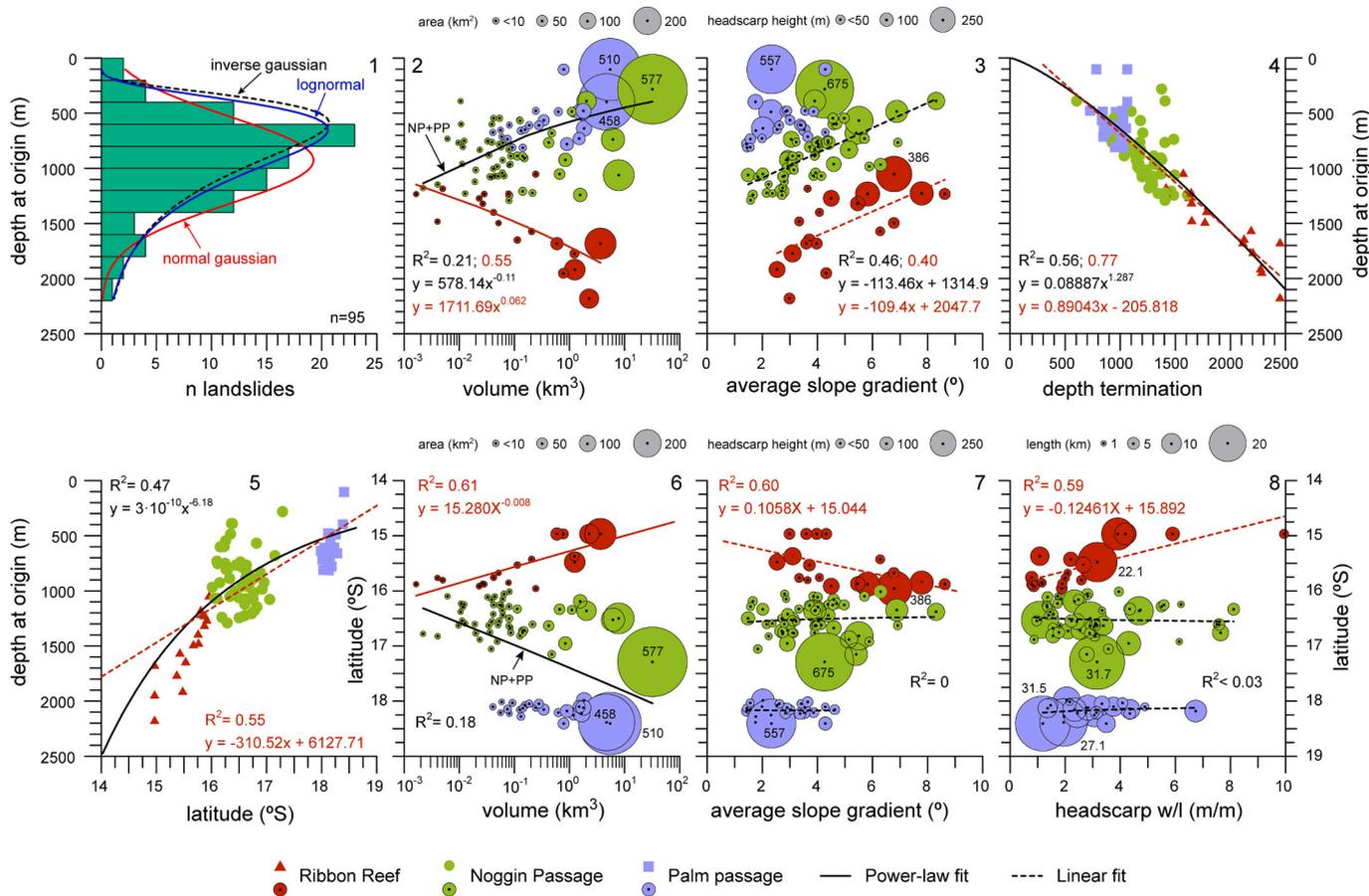
Fig. 10. Histogram and scatter plots showing the variation of selected landslide parameters against depth at origin (1–4) and latitude (5–8). In 2–4 and 6–8, the diameter of the circles is scaled to the parameter indicated in the plot. Regression lines and corresponding equation to a power-law and/or linear fit (continuous and dashed lines, respectively) and coefficient of determination (R^2) are given for plot 2–8. Colour of R^2 and equations corresponds to the distribution fit shown in the plot.

Table 3

Spearman's ρ rank correlation coefficients between the main morphological parameters of the submarine landslides on the GBR margin of NE Australia. High correlation coefficient (ρ > 0.7 and < −0.7) are highlighted in bold and moderate correlations ((ρ = 0.5–0.7 and −0.5–(−0.7)) are in cursive. This dataset includes landslide complexes and individual landslides within complex (N = 95).

	L_t	L_s	W	W_e	A	V	V/h_w	T_d	T_{fs}	D_o	D_t	H	H_s	h_h	h_g	S_o	S_a	S_{ad}	S_{ev}	H/L	h_p	h_w	h_l	$h_{w/l}$	h_s	Sh_f
L_t	1																									
L_s	**0.84**	1																								
W	0.61	0.67	1																							
W_e	0.62	0.68	1.00	1																						
A	**0.86**	**0.77**	**0.92**	**0.92**	1																					
V	**0.78**	**0.71**	**0.87**	**0.87**	**0.93**	1																				
V/h_w	**0.81**	**0.71**	*0.61*	*0.62*	**0.78**	**0.90**	1																			
T_d	0.35	0.28	0.49	*0.50*	0.47	**0.74**	**0.77**	1																		
T_{fs}	**0.86**	**0.77**	**0.92**	**0.92**	**1.00**	**0.93**	**0.78**	0.47	1																	
D_o	−0.16	*−0.55*	−0.23	−0.22	−0.20	−0.22	−0.17	−0.19	−0.20	1																
D_t	0.22	−0.21	0.05	0.05	0.14	0.13	0.21	0.07	0.14	**0.82**	1															
H	**0.71**	**0.75**	*0.50*	*0.50*	*0.65*	*0.67*	**0.73**	0.49	*0.65*	−0.26	0.23	1														
H_s	0.36	*0.62*	0.26	0.27	0.31	0.38	0.46	0.32	0.31	−0.30	0.18	**0.94**	1													
h_h	0.27	0.24	0.22	0.23	0.26	0.39	0.43	*0.52*	0.26	−0.14	0.18	*0.56*	*0.54*	1												
h_g	0.13	0.10	0.02	0.03	0.06	0.18	0.31	0.40	0.06	−0.22	0.08	*0.50*	0.48	*0.52*	1											
S_o	−0.13	−0.03	−0.25	−0.25	−0.24	−0.21	−0.08	0.01	−0.24	−0.25	−0.08	0.25	0.44	0.38	*0.56*	1										
S_a	−0.45	−0.21	−0.27	−0.26	−0.39	−0.29	−0.24	0.11	−0.39	−0.09	−0.04	0.17	*0.53*	0.27	0.42	*0.52*	1									
S_{ad}	*−0.53*	−0.41	−0.36	−0.37	*−0.48*	−0.44	−0.36	−0.03	*−0.48*	−0.05	−0.09	0.03	0.30	0.20	0.44	*0.61*	**0.92**	1								
S_{ev}	−0.43	−0.28	−0.38	−0.37	−0.45	−0.45	−0.37	−0.25	−0.45	−0.05	−0.11	0.07	0.24	−0.05	0.32	0.38	**0.76**	**0.72**	1							
H/L	**−0.70**	−0.41	−0.37	−0.37	*−0.56*	−0.46	−0.44	−0.04	*−0.56*	−0.04	−0.10	−0.03	0.35	0.15	0.27	0.46	**0.84**	**0.81**	**0.75**	1	–					
h_p	*0.57*	*0.61*	**0.95**	**0.94**	**0.86**	**0.85**	*0.60*	*0.55*	**0.86**	−0.27	0.01	0.50	0.23	0.36	0.06	−0.18	−0.20	−0.32	−0.39	−0.32	1					
h_w	0.55	0.58	**0.97**	**0.97**	**0.87**	**0.85**	0.56	0.52	**0.87**	−0.23	0.01	0.44	0.17	0.27	0.02	−0.24	−0.24	−0.35	−0.40	−0.34	**0.97**	1				
h_l	*0.60*	*0.59*	**0.74**	**0.74**	**0.75**	**0.78**	*0.66*	*0.57*	**0.75**	−0.19	0.09	*0.55*	0.32	*0.51*	0.11	−0.16	−0.15	−0.29	−0.34	−0.31	**0.84**	**0.75**	1			
$h_{w/l}$	0.03	0.07	*0.51*	*0.50*	0.33	0.25	−0.06	0.02	0.33	−0.04	−0.08	−0.08	−0.18	−0.27	−0.17	−0.23	−0.13	−0.14	−0.14	−0.08	0.39	*0.54*	−0.10	1		
h_s	0.08	−0.02	−0.25	−0.26	−0.13	−0.06	0.18	0.08	−0.13	−0.05	0.05	0.17	0.11	0.26	0.13	0.21	0.08	0.08	0.04	0.04	−0.08	−0.28	0.27	**−0.80**	1	
Sh_f	−0.24	−0.07	*0.57*	*0.57*	0.25	0.28	−0.03	0.28	0.25	−0.10	−0.13	−0.12	−0.06	0.00	−0.14	−0.16	0.09	0.06	−0.08	0.23	*0.56*	*0.61*	0.32	*0.54*	−0.31	1

D_o: depth at origin; D_t: depth at termination; L_t: total length. L_s: length on the slope; W: maximum width; W_e: maximum width of the evacuated area; A: area; V: volume; V/h_w: volume/headscarp width; T_d: average thickness of the deposit given as V/A; T_{fs}: average thickness of the failed section (given as $A^{0.27}$; Klar et al., 2011); H: total height from D_o to D_t; H_s: height from D_0 to the base of the slope; S_o: slope gradient at origin; S_a: average slope gradient; S_{ad}: slope of the adjacent unfailed slope; S_{ev}: slope of the evacuated area; H/L: ratio total height/total length; h_h: headscarp height; h_g: headscarp slope gradient; h_p: headscarp perimeter; h_w: headscarp width; h_l: headscarp length; $h_{w/l}$: ratio headscarp width/headscarp length; h_s: headscarp sinuosity; Sh_f: shape factor (A/L_t^2).

formed at slopes with average gradients steeper than the mean for the full dataset (Fig. 9-8; Table 2).

The perimeter and width of the landslide scar are not clearly related with the incision along the headscarp (i.e., headscarp height) ($\rho = 0.36$ and 0.27, respectively) (Table 3) (e.g., Urgeles and Camerlenghi, 2013) and these variables do not fit well to any regression line ($R^2 < 0.2$) (Supplementary data 5-30). However, the perimeter of the scars is generally larger for a given scarp height in the PP region than in NP region (Supplementary data 5-30; 8).

The H/L ratio, which is commonly used to characterize landslide mobility (e.g., Hampton et al., 1996), shows negative correlation with the landslide dimensions ($\rho = -0.37$–(-0.56)) (Table 3). The dependence of this ratio with the average thickness of the deposits is almost null ($\rho = -0.04$) (Table 3). The landslides in the RR region have, in general, slightly higher H/L ratios for equivalent size in NP and PP regions (Supplementary data 5-6, -11).

The general relationships found among the different morphometric parameters for the full landslide database are overall reflected in similar relationships in the different landslide types (see Supplementary data 7). In slope-detached landslides, the headscarp gradient is better correlated with the slope gradient at origin ($\rho = 0.69$), suggesting a relatively dependant depth of headscarp incision in this type of landslides ($R^2 = 0.58$ for a linear regression). In the case of the intra-slope landslides, the depth at origin has relatively significant negative correlation with the landslide height ($\rho = -0.72$), and the height/length ratio shows higher correlation with the headscarp gradient ($\rho = 0.43$) ratio compared with the full dataset ($\rho = 0.27$), as this ratio is similar to the average unfailed slope (Table 3; Supplementary data 7). Although the number of landslide complexes is low ($n = 12$), some dimensional dependences are much stronger in these landslide complexes than those found for the full dataset. For example, volume and height ($\rho = 0.91$; $R^2 = 0.71$ for a power-law fit) or H/L ratio with the area ($\rho = -0.78$ and $R^2 = 0.59$) and volume ($\rho = -0.73$ and $R^2 = 0.66$) (Supplementary data 6 and 7).

The depth distribution of the landslides shows a rather moderate relationship with their latitudinal location along the margin ($R^2 = 0.47$–0.55) (Fig. 10-5). The latitudinal variation of the landslide size, average slope gradient and some characteristics of the headscarps show poor to nil correlation with any regression fit in the NP and PP regions ($R^2 < 0.18$) (Fig. 10-6–8). In contrast, moderate fits ($R^2 \sim 0.60$) are observed in the RR region, suggesting that some of the landslides morphometric characteristics could be dependent on the regional setting.

4.4. Size-frequency distribution

Our results confirm that the landslide volume does not fit either to an inverse power law, logarithmic or exponential distribution for the full dataset, but from the volume cut-off threshold (see Methods Section 3.3) it displays a distribution between an inverse power law ($R^2 = 0.957$) and a logarithmic function ($R^2 = 0.909$) (Fig. 11). The power-law function fits over four orders of magnitude (~ 0.03–32 km^3; number of landslides $= 15.33 V_L^{-0.47}$) to the landslide volume distribution, and over three orders of magnitude (~ 0.03–4 km^3; number of landslides $= 13.07 \ln(V_L) + 19.30$) in the case of the logarithmic function (Fig. 11A; Table 4). A lognormal distribution with $\mu = -2.110$ and $\sigma = 1.950$ fits very well to the full dataset over four orders of magnitude (Fig. 11A; Table 4).

The probability distribution of the landslide volume can also be fitted by an inverse power-law distribution with a scaling parameter (α) of 1.49 (Fig. 12). The p value goodness-of-fit estimator is 0.11 (Table 4), which indicates that the fitting to an inverse power-law distribution is
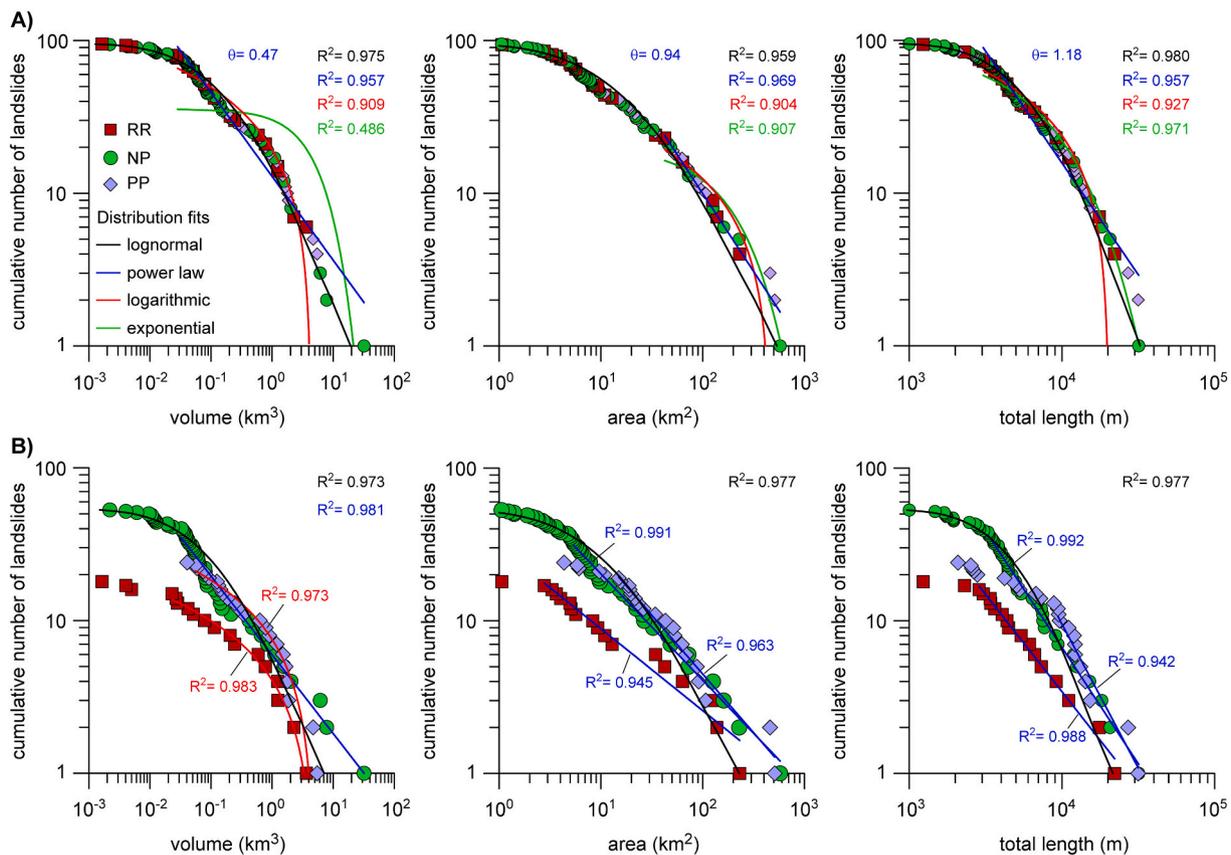
Fig. 11. Plots of cumulative volume, area and total length distributions of submarine landslide on the GBR margin (A) and by regions in the margin (B). Regression lines (from the cut-off threshold) for a power-law, logarithmic and exponential fit, the lognormal distribution fit for the full dataset (for distributions with number of landslides > 50) and corresponding coefficient of determination (R^2) are given for each plot. The scaling parameter (θ) of the inverse power-law distribution is also given. Legend in A is also for B.

Table 4
Statistics of landslide volume (V) cumulative distribution on the Great Barrier Reef (GBR) margin and its relationship to different types of distribution functions (see text). All distributions are fitted from the lower cut-off threshold unless indicated.

Dataset	$N_L = aV^{-\theta}$					$N_L = -\gamma ln(V) + b$			$N_L = ce^{-\varphi V}$			$N_L^* = 0.5 \cdot erfc \cdot ((-lnV-\mu)/\sigma 2^{0.5})$			$N_L = 0.5 \cdot erfc \cdot ((-lnV-\mu)/\sigma 2^{0.5})$			α
	a	θ	R²	a*	θ*	b	γ	R²	c	φ	R²	μ	σ	R²	μ	σ	R²	
Region																		
GBR	12.89	0.55	0.957	15.33	0.47	19.30	13.07	0.909	35.67	0.1661	0.486	−2.110	1.950	0.991	−1.507	1.621	0.975	1.49
Ribbon Reef	3.33	0.43	0.899	4.12	0.34	4.07	2.56	0.983	10.69	0.7228	0.924	–	–	–	–	–	–	1.45
Noggin Passage	5.97	0.52	0.981	3.74	0.69	9.08	6.06	0.757	18.48	0.1149	0.469	−2.551	1.880	0.985	−1.884	1.657	0.973	1.65
Palm Passage	5.57	0.56	0.909	6.84	0.43	7.52	4.72	0.973	15.99	0.5416	0.886	–	–	–	–	–	–	1.52
Landslide type																		
SD	5.10	0.52	0.953	5.66	0.47	4.65	7.00	0.912	15.15	0.3905	0.762	–	–	–	–	–	–	1.53
IS	0.02	1.76	0.931	0.01	2.23	−11.81	5.59	0.775	13.90	22.3663	0.840	–	–	–	–	–	–	4.00
C. ind.	4.52	0.59	0.944	5.72	0.49	5.30	6.24	0.933	18.84	0.8161	0.794	–	–	–	–	–	–	1.52
C	4.52	0.59	0.944	6.90	0.66	5.30	6.24	0.933	18.84	0.8161	0.794	–	–	–	–	–	–	2.03
SD + C	9.15	0.47	0.942	11.37	0.36	13.14	6.08	0.948	18.96	0.1229	0.568	–	–	–	–	–	–	1.40
SC + IS+C. ind.	8.73	0.61	0.956	9.77	0.56	11.75	12.26	0.891	35.79	0.5741	0.748	−2.375	1.804	0.944	−1.733	1.445	0.970	1.59
S + IS+C	9.21	0.49	0.961	10.31	0.43	13.62	7.33	0.906	22.56	0.1332	0.530	−2.019	2.089	0.996	−1.415	1.760	0.989	1.47

	X_min (km³)	Max. (km³)	Interval (X_min-Max.) (km³)	n_pw (n)	p	PwL	Power law vs lognormal				Power law vs exponential			
							Test statistics	p_one side	p_two sides	Stat. Equal	Test statistics	p_one side	p_two sides	Stat. Equal
Region														
GBR	0.028	32	0.0284–32	77 (95)	0.11	Yes	−1.340	0.910	0.181	Yes	2.900	0.0019	0.0038	No
Ribbon Reef	0.023	3.64	0.0229–3.64	13 (18)	0.19	Yes	−0.329	0.629	0.742	Yes	0.892	0.186	0.372	Yes
Noggin Passage	0.033	32	0.0326–0.32	40 (53)	0.15	Yes	0.078	0.469	0.938	Yes	4.110	1.94·10⁻⁵	3.89·10⁻⁵	No
Palm Passage	0.056	5.48	0.0561–5.48	23 (24)	0.08	Yes	−0.720	0.764	0.472	Yes	0.823	0.205	0.411	Yes
Landslide type														
SD	0.038	7.80	0.0381–7.88	26 (28)	0.25	Yes	−0.422	0.663	0.673	Yes	2.33	0.01	0.02	No
IS	0.039	0.13	0.0326–0.13	8 (17)	0.87	Yes	0.241	0.405	0.810	Yes	0.747	0.228	0.455	Yes
C. ind.	0.027	4.69	0.0268–4.69	31 (38)	0.06	Yes	−1.030	0.848	0.304	Yes	1.480	0.0697	0.139	No
C	1.787	32	1.7875–32	5 (12)	0.81	Yes	0.323	0.373	0.747	Yes	1.010	0.157	0.314	Yes
SD + C	0.028	32	0.0284–32	38 (40)	0.05	Yes	−0.763	0.777	0.445	Yes	3.550	0.0002	0.0004	No
SC + IS + C. ind.	0.033	7.80	0.0326–7.8	65 (83)	0.11	Yes	−1.340	0.910	0.181	Yes	2.900	0.0019	0.0038	No
S + IS + C	0.028	32	0.0284–32	47 (57)	0.1	Yes	−0.770	0.779	0.441	Yes	2.950	0.0016	0.0032	No

SD: slope-detached landslides; IS: intra-slope landslides; C. ind.: individual landslides within a landslide complex (C).

a*, θ*: values correspond the NLS (nonlinear least squares) fitting.

N_L^*: number of landslides using all the observed values.

erfc: complementary error function.

μ, σ: location and shape parameter, respectively, of the probability density function for the lognormal distribution.

α: scaling exponent of the power-law cumulative probability distribution function.

X_min: cut-off threshold. Lower value considered in distribution fit.

Max.: maximum observed value.

n_pw: number of data considered used for the distribution fit out of the total observations in brackets.

p: goodness of fit estimator to a power-law distribution (Kolmogorov-Smirnov statistic test).

PwL: distribution explained by a power-law function.

Stat. Equal: compared distributions are both statistically significant. No means the power-law distribution is preferred.

Fig. 12. Plot of the cumulative distribution function of volume for landslides in the GBR margin and comparison with the Gioia Basin (Tyrrhenian Sea; Casas et al., 2016). Different fits to the distribution from the cut-off threshold are shown (0.025 km³). The probability of reaching the volume of the median volume of the dataset (0.081 km³) and large landslides (>5 km³) based on power-law and lognormal fits is also indicated.

plausible. The test statistic (likelihood ratio test) between the power-law and the lognormal functions is −1.34. This negative value may suggest that the lognormal distribution is slightly more significant, but either the p-one side or p-two sides (>0.05–0.1; Table 4) indicate both power-law and lognormal distributions are statistically equal and that one model cannot be favoured over the other. In contrast, the likelihood ratio test between the power-law and the exponential functions confirms that both distributions are statistically different (p-one side or p-two sides <0.05; Table 4). Among regions (RR, NP, and PP), the landslide volume distributions show scaling parameters of 0.34–0.69 to a power law, and in the case of NP region, a lognormal distribution with μ = −2.551 and σ = 1.880 (Table 4). The likelihood ratio test reflects a similar behaviour to the full dataset (Fig. 11B). In all regions, the landslide volume distribution can be explained statistically by both power-law and lognormal functions. However, only in the NP region, the exponential function can be discarded. In the RR and PP regions, the power-law function cannot be favoured over the exponential function. This might be related to the lower number of landslides in the RR and PP regions. Considering the different landslide types, the results are overall comparable with the full dataset (Table 4).

Cumulative area distribution fits power-law ($R^2 = 0.969$), logarithmic ($R^2 = 0.904$) and exponential ($R^2 = 0.907$) functions over the largest two orders of magnitude (42.4–576.6 km²) (Fig. 11A; Table 5). The lognormal fit to the full dataset covers the lower two orders of magnitude with μ = −2.584 and σ = 1.450 (Fig. 11A; Table 5). The exponent of the power-law fitting is 0.94 and the p value goodness-of-fit estimator (0.530) indicates that such a distribution is possible. Both the ratio of the likelihood between the power-law and the lognormal functions and between the power-law and the exponential functions are statistically equal, and thus one model cannot be favoured over the other. However, the relatively low number of landslides ($n = 23$) above the lower bound of the tail may influence the statistics. There is a trend in the power-law scaling behaviour of the landslide area among different regions,

increasing from north (θ = 0.50) to south (θ = 0.73) (Table 5), otherwise lower than the exponent for the full dataset. Considering the different landslide types, the slope-detached landslides are the only ones that do not follow a power-law distribution (p value of 0.04) (Table 5).

The total length of the landslides is well explained by a lognormal distribution with μ = 8.546 and σ = 0.737 ($R^2 = 0.98$) (Fig. 11A; Table 6). The cumulative distribution from the lower bound tail can be fitted to power-law, logarithmic and exponential functions with similar high R^2 values (Fig. 11A; Table 6). However, the p value estimator (0.04) suggests the fitting to power law is statistically unlikely, and therefore, another distribution such as exponential is more plausible. In contrast, the power-law function can explain the cumulative landslide length distribution by regions, with an increasing scaling exponent from north to south (θ = 1.19 to 2.19) (Fig. 11B; Table 6). By region and landslide types, the likelihood ratio test suggests that power-law and lognormal distributions are statistically equal for our dataset, being impossible to differentiate between them. On the other hand, the power-law and the exponential distributions are, in general, different for our dataset, commonly favouring the power-law over the exponential distribution (Table 6).

5. Discussion

5.1. Slope failure dynamics

In this section, we have used the information extracted from the relationships between landslide morphometric parameters and ratios, and/or the magnitude-frequency distributions, to infer the sedimentary processes involved in the movement and deposition of slope failures on the GBR margin. This morphometric approach represents a first step to evaluate slope failure dynamics (McAdoo et al., 2000; Canals et al., 2004; Hühnerbach et al., 2004; Chaytor et al., 2009; Casalbore et al., 2011; Urgeles and Camerlenghi, 2013), which could be tested and/or

Table 5
Statistics of landslide area (A) cumulative distribution on the Great Barrier Reef (GBR) margin and its relationship to different types of distribution functions (see text). All distributions are fitted from the lower cut-off threshold unless indicated.

Dataset	$N_L = aA^{-\theta}$					$N_L = -\gamma ln(A) + b$			$N_L = ce^{-\varphi A}$			$N_L^* = 0.5 \cdot erfc \cdot ((-lnA-\mu)/\sigma 2^{0.5})$			$N_L = 0.5 \cdot erfc \cdot ((-lnA-\mu)/\sigma 2^{0.5})$			α
	a	θ	R²	a*	θ*	b	γ	R²	c	φ	R²	μ	σ	R²	μ	σ	R²	
Region																		
GBR	1086.7	1.02	0.969	758.7	0.94	49.63	8.08	0.904	20.29	0.0051	0.907	2.584	1.450	0.954	4.658	0.781	0.959	2.10
Ribbon Reef	30.5	0.54	0.945	28.2	0.50	17.48	3.21	0.930	11.23	0.0114	0.904	–	–	–	–	–	–	1.60
Noggin Passage	100.8	0.70	0.991	98.1	0.69	17.90	0.01	0.692	17.90	0.0066	0.692	2.199	1.366	0.980	2.965	2.965	0.977	1.78
Palm Passage	154.9	0.77	0.963	135.9	0.73	29.68	5.09	0.868	12.45	0.0050	0.758	–	–	–	–	–	–	1.87
Landslide type																		
SD	69.0	0.64	0.939	48.6	0.49	31.63	6.16	0.966	19.12	0.0144	0.913	–	–	–	–	–	–	1.54
IS	64.2	1.62	0.964	47.6	1.39	18.18	7.55	0.927	21.69	0.2710	0.958	–	–	–	–	–	–	2.7598
C. ind.	163.3	0.86	0.905	2290	1.51	16.04	2.63	0.700	6.16	0.0043	0.734	–	–	–	–	–	–	2.5797
C	129.1	0.71	0.934	86.5	0.62	16.97	3.03	2.506	7.57	0.0032	0.923	–	–	–	–	–	–	1.87
SD + C	1113.9	1.06	0.967	893.8	1.01	45.61	7.82	0.980	12.41	0.0043	0.913	–	–	–	–	–	–	2.31
SC + IS + C. ind.	218.0	0.78	0.972	758.7	0.49	78.45	16.24	0.914	38.71	0.0117	0.738	2.351	1.303	0.995	2.715	1.143	0.987	1.70
S + IS + C	103.8	0.58	0.949	81.2	0.46	54.89	10.00	0.943	30.47	0.0071	0.786	2.625	1.555	0.955	2.790	1.486	0.961	1.51

	X_{min} (km²)	Max. (km²)	Interval (X_{min}-Max) (km²)	n_{pw} (n)	p	PwL	Power law vs lognormal				Power law vs exponential			
							Test statistics	p_one side	p_two sides	Stat. Equal	Test statistics	p_one side	p_two sides	Stat. Equal
Region														
GBR	42.4	576.6	42.4–576.6	23 (95)	0.53	Yes	−0.248	0.598	0.805	Yes	0.962	0.168	0.336	Yes
Ribbon Reef	2.8	231.1	2.8–231.1	17 (18)	0.45	Yes	−0.173	0.569	0.863	Yes	1.580	0.0572	0.114	Yes
Noggin Passage	5.4	576.6	5.4–576.6	32 (53)	0.64	Yes	−0.029	0.511	0.977	Yes	2.450	0.007	0.014	No
Palm Passage	15.0	509.5	15.0–509.5	19 (24)	0.33	Yes	−0.143	0.557	0.886	Yes	1.630	0.052	0.104	Yes
Landslide type														
SD	2.8	228.6	2.8–228.6	27 (28)	0.04	No	−1.110	0.867	0.266	Yes	0.625	0.266	0.532	Yes
IS	2.7	11.9	2.7–11.9	12 (17)	0.29	Yes	−0.181	0.572	0.856	Yes	−0.369	0.644	0.712	Yes
C. ind.	42.4	458.1	42.4–458.1	8 (38)	0.84	Yes	0.159	0.437	0.873	Yes	1.880	0.030	0.061	No
C	45.8	576.6	45.8–576.6	8 (12)	0.28	Yes	0.026	0.490	0.979	Yes	0.114	0.455	0.909	Yes
SD + C	72.5	576.6	72.5–576.6	12 (40)	0.72	Yes	0.038	0.485	0.970	Yes	0.498	0.309	0.618	Yes
SC + IS + C. ind.	3.6	458.1	3.6–458.1	67 (83)	0.04	No	−1.140	0.873	0.253	Yes	2.090	0.0183	0.0366	No
S + IS + C	2.3	576.6	2.3–576.6	53 (57)	0.10	Yes	−1.190	0.882	0.236	Yes	2.550	0.0054	0.0107	No

SD: slope-detached landslides; IS: intra-slope landslides; C. ind.: individual landslides within a landslide complex (C).

a*, θ*: values correspond the NLS fitting.

N_L^*: number of landslides using all the observed values.

erfc: complementary error function.

μ, σ: location and shape parameter, respectively, of the probability density function for the lognormal distribution.

α: scaling exponent of the power-law cumulative probability distribution function.

X_{min}: cut-off threshold. Lower value considered in distribution fit.

Max.: maximum observed value.

n_{pw}: number of data considered used for the distribution fit out of the total observations in brackets.

p: goodness of fit estimator to a power-law distribution (Kolmogorov-Smirnov statistic test).

PwL: distribution explained by a power-law function.

Stat. Equal: compared distributions are both statistically significant. No means the power-law distribution is preferred.
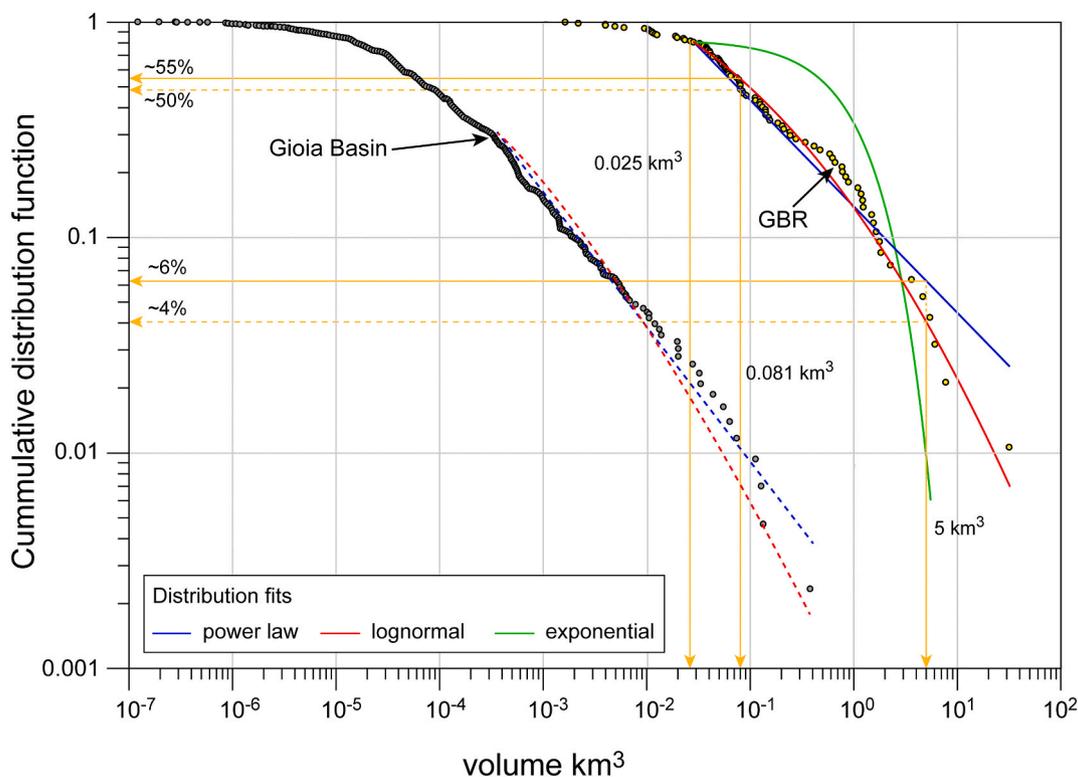
Table 6
Statistics of landslide length (L) cumulative distribution on the Great Barrier Reef (GBR) margin and its relationship to different types of distribution functions (see text). All distributions are fitted from the lower cut-off threshold unless indicated.

Dataset	$N_L = aL^{-\theta}$					$N_L = -\gamma\ln(L) + b$			$N_L = ce^{-\varphi L}$			$N_L^* = 0.5 \cdot erfc \cdot ((-\ln L - \mu)/\sigma 2^{0.5})$			$N_L = 0.5 \cdot erfc \cdot ((-\ln L - \mu)/\sigma 2^{0.5})$			α
	a	θ	R^2	a*	θ*	b	γ	R^2	c	φ	R^2	μ	σ	R	μ	σ	R^2	
Region																		
GBR	$1.12 \cdot 10^7$	1.46	0.957	$9.96 \cdot 10^5$	1.18	332.46	33.51	0.927	90.76	0.00014	0.971	8.546	0.737	0.988	8.81	0.601	0.980	2.27
Ribbon Reef	$4.21 \cdot 10^5$	1.27	0.988	$2.17 \cdot 10^5$	1.19	72.29	7.36	0.908	18.38	0.00014	0.942	–	–	–	–	–	–	2.41
Noggin Passage	$8.39 \cdot 10^6$	1.52	0.992	$1.94 \cdot 10^7$	1.63	173.96	17.80	0.827	41.27	0.00014	0.901	8.380	0.691	0.972	8.672	0.550	0.946	2.74
Palm Passage	$3.29 \cdot 10^8$	1.88	0.942	$5.58 \cdot 10^9$	2.19	85.16	8.26	0.796	23.34	0.00010	0.891	–	–	–	–	–	–	3.68
Landslide type																		
SD	$1.34 \cdot 10^6$	1.32	0.901	$4.81 \cdot 10^4$	0.93	125.43	12.60	0.980	39.43	0.00015	0.982	–	–	–	–	–	–	2.08
IS	$9.96 \cdot 10^{19}$	2.83	0.979	$3.81 \cdot 10^{12}$	3.28	111.90	12.62	0.854	64.14	0.00057	0.965	–	–	–	–	–	–	4.90
C. ind.	$7.51 \cdot 10^6$	1.56	0.795	$2.57 \cdot 10^{19}$	4.70	43.21	4.20	0.575	10.19	0.00009	0.727	–	–	–	–	–	–	4.92
C. ind.	$1.22 \cdot 10^7$	1.54	0.906	$4.94 \cdot 10^6$	1.45	56.54	5.35	0.900	16.04	0.00008	0.891	–	–	–	–	–	–	2.85
SD + C	$3.48 \cdot 10^2$	2.31	0.967	$3.66 \cdot 10^{10}$	2.32	130.16	12.59	0.878	47.20	0.00011	0.947	–	–	–	–	–	–	3.93
SC + IS + C.ind.	$7.56 \cdot 10^6$	1.50	0.952	$4.98 \cdot 10^6$	1.40	177.28	18.13	0.932	52.17	0.00017	0.976	8.429	0.673	0.991	8.734	0.531	0.977	2.57
S + IS + C	$3.49 \cdot 10^{10}$	2.31	0.967	$3.66 \cdot 10^{10}$	2.32	130.16	12.59	0.878	47.20	0.00011	0.947	8.723	0.725	0.987	8.901	0.628	0.985	3.93

	X_{min} (m)	Max. (m)	Interval (X_{min}-Max.) (m)	n_{pw} (n)	p value	Power law	Power law vs lognormal				Power law vs exponential			
							Test statistics	p_one side	p_two sides	Stat. Equal	Test statistics	p_one side	p_two sides	Stat. Equal
Region														
GBR	3048	31,763	3048–31,763	73 (95)	0.04	No	−1.490	0.932	0.136	Yes	3.670	0.0001	0.0002	No
Ribbon Reef	2867	22,128	2867–22,128	16 (18)	0.83	Yes	−0.160	0.564	0.873	Yes	1.210	0.114	0.227	Yes
Noggin Passage	3284	31,763	3284–31,763	38 (53)	0.70	Yes	−0.020	0.508	0.984	Yes	2.070	0.0193	0.0385	No
Palm Passage	9388	31,559	9388–31,559	12 (24)	0.45	Yes	0.215	0.415	0.83	Yes	1.310	0.096	0.191	Yes
Landslide type														
SD	2867	22,128	2867–22,128	26 (28)	0.000	No	−1.170	0.879	0.242	Yes	2.510	0.006	0.012	No
IS	3284	7338	3284–7338	12 (17)	0.87	Yes	0.194	0.423	0.846	Yes	0.319	0.375	0.750	Yes
C. ind.	8840	27,094	8840–27,094	7 (38)	0.62	Yes	0.138	0.445	0.890	Yes	0.737	0.230	0.461	Yes
C. ind.	9427	31,763	9427–31,763	8 (12)	0.36	Yes	0.046	0.482	0.963	Yes	1.350	0.088	0.177	No
SD + C	11,446	31,763	11,446–31,763	15 (40)	0.67	Yes	0.150	0.440	0.881	Yes	1.580	0.057	0.114	No
SC + IS + C.ind.	3284	22,128	3284–22,128	59 (83)	0.26	Yes	−0.798	0.788	0.425	Yes	3.380	0.000	0.001	No
S + IS + C	11,446	31,763	11,446–31,763	15 (57)	0.67	Yes	0.150	0.440	0.881	Yes	1.580	0.057	0.114	No*

SD: slope-detached landslides; IS: intra-slope landslides; C. ind.: individual landslides within a landslide complex (C).

a*, θ*: values correspond the NLS fitting.

N_L^*: number of landslides using all the observed values.

erfc: complementary error function.

μ, σ: location and shape parameter, respectively, of the probability density function for the lognormal distribution.

α: scaling exponent of the power-law cumulative probability distribution function.

X_{min}: cut-off threshold. Lower value considered in distribution fit.

Max.: maximum observed value.

n_{pw}: number of data considered used for the distribution fit out of the total observations in brackets.

p: goodness of fit estimator to a power-law distribution (Kolmogorov-Smirnov statistic test).

PwL: distribution explained by a power-law function.

Stat. Equal: compared distributions are both statistically significant. No means the power-law distribution is preferred.

better characterized to obtain ground-truthing of the interpretations where its integration with subseafloor seismic data and information of geotechnical parameters from sediment cores or images from ROV is possible (Chaytor et al., 2016; Li et al., 2017; Locat, 2019)

5.1.1. Type of mass movement

McAdoo et al. (2000) found that submarine blocky landslides in the U.S. continental slope tend to have large h_h/L_t ratios, and slumps have a slightly larger h_h/L_t ratio than fluid (disintegrative) ones. When plotting the GBR dataset against the ratios that define such landslide types on the North American margin, about one third corresponds to blocky landslides (Fig. 13). The rest corresponds to disintegrative landslides (37%) and slope failures that could be assigned to blocky landslides or slumps (32%) (Fig. 13). The correlation between h_h and L_t increases significantly when blocky, blocky-slump and disintegrative landslides are plotted separately ($R^2 = 0.74, 0.96$ and 0.83, respectively against $R^2 = 0.27$ for the full dataset) (Fig. 13 and Supplementary data 5-27). Although the h_h/L_t ratio that defines blocky, slumps and disintegrative landslides may depend on local or regional factors, and may vary from one margin to another, we consider that the ratios presented by McAdoo et al. (2000) are a good preliminary morphological indicator to differentiate the landslide types.

Micallef et al. (2008) argued that the headscarp shape (ratio between the headscarp width (h_w) and length (h_l)) can be used as a proxy for the type of mass movement (spreads or debris flow). These authors suggest that headscarps formed by spreads have approximate h_w/h_l ratios >4 and their shapes range between cauliflower-shaped and linear. In contrast, headscarps formed by debris flows are more curvilinear and have h_w/h_l ratio < 4. Following this approach, we found that most of the GBR headscarps were formed by debris flows as suggested by the overall headscarp morphology, and the mean (3.14 ± 1.86) and frequency distribution of the h_w/h_l ratio (Fig. 14). There are not significant differences by regions, suggesting that headscarp crumbling by debris

flows is the dominant process along the entire GBR margin. Note, however, that Micallef et al. (2008) did not differentiate between debris flow and other mass failures that may evolve into debris flow downslope (e.g., slumps). The comparison of the headscarp shapes and h_w/h_l ratios in the GBR landslides with other selected examples (Fig. 14) suggests that spreading is uncommon outside glaciated margins independently of their volume (Fig. 14). Along the GBR margin, the only submarine landslide that shows evidence of spreading is the Viper Slide (Puga-Bernabéu et al., 2020), which has a distinct linear headscarp with a high h_w/H_h ratio (7.5) (Fig. 14). This slope failure involved the collapse of part of the shelf edge that included coral reef build-ups (Webster et al., 2016), which suggests a rather rigid and coherent pre-failure mass. GBR landslides included in this dataset, with a few exceptions (e.g., Bowl Slide, Puga-Bernabéu et al., 2020), did not affect the shelf edge that could include coral reefs, and therefore, the formation of landslide headscarps by spreading is rather uncommon over the ~500 km length of the margin investigated.

5.1.2. Landslide mobility

The mobility of slope failures has commonly been assessed using the relationship between the height/total length ratio (H/L) (apparent friction angle) and the landslide volume (V) (Hampton et al., 1996; Moernaut and De Batist, 2011; Calvès et al., 2015). However, Davies (1982) proposed that rock avalanche debris mobility (total length; Lt) is primarily controlled by its volume, with height being a secondary factor that introduces scatter to the correlation. We compared the landslide mobility given by the two approaches (H/L-V and L_t-V) (Figs. 15 and 16).

The GBR landslides fall within the common mobility field for subaqueous debris flows according to De Blasio et al. (2006) (H/L-V plot), and most of them fall between the submarine landslides boundaries from Hampton et al. (1996) and Edgers and Karlsrud (1982) (Fig. 15). Some landslides are on or close to the boundary with the fields of subaerial and subaqueous rock avalanches, including the largest landslide in the GBR (Gloria Knolls Slide; Puga-Bernabéu et al., 2017). This suggests that those landslides may have a rheological behaviour close to rock avalanches, and presumably, with relatively low mobility. The H/L ratio of the GBR landslides ranges between 0.016 and 0.152, but this ratio is within a relatively narrow interval (0.024–0.035) for the five largest landslides (volume > 4.5 km^3) (Fig. 15). This could imply that given a relatively large size, then landslide mobility could be relatively independent of the volume of the slide mass. The power-law regression fit for the GBR landslides plots parallel to the lower boundary of Edgers and Karlsrud (1982), although relatively far from it (Fig. 15). In contrast, this power-law regression fit cross-cuts the upper boundary of Hampton et al. (1996) at larger sizes (Fig. 15), suggesting that the mobility of the larger GBR landslides may be relatively reduced compared with smaller ones. Considering the potential landslide mobility inversely given by the H/L ratio, the Gloria Knolls Slide shows relatively low mobility (H/L ratio = 0.035) compared with other landslides of similar sizes, such as the BIG'95 and Gondola slides with ratios <0.013 (Fig. 15) (Lastras et al., 2004a; Dalla Valle et al., 2015).

The power-law regression line that fits the L_t-V relationship in the GBR landslides has exponent values of 0.31 (full dataset) and 0.33 (slope-detached landslides + complexes), with coefficients of determination R^2 of 0.69 and 0.79, respectively, which indicates a good relationship between both variables (Fig. 16A). When plotting the selected examples of other landslides worldwide (same examples as in Fig. 15), most of them fall over or close to the power-law regression line for the GBR landslides independent of their sizes (Fig. 16A). This suggests that the runout distance of the landslides could be primarily controlled by their volume regardless of the type of mass movement (i.e., rock and debris avalanches, slides, debris flow, etc.) and that the height drop may be just conditioned by the margin physiography where landslides occur (Legros, 2002; Moernaut and De Batist, 2011). Only in particular cases, the L_t-V relationship veers from the general GBR trend (Fig. 16A). For
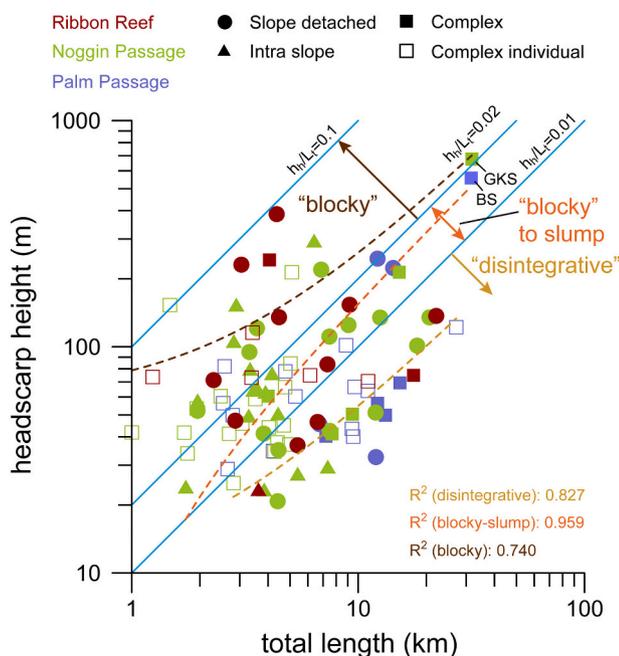
Fig. 13. Graph of headscarp height against total length (runout) for the submarine landslides on the GBR margin. Trends in blue correspond to the ratios between the two parameters (h_h/L_t). The division between blocky and disintegrative failures according to McAdoo et al. (2000) is marked ($h_h/L_t = 0.01$). Regression lines to a linear fit (dashed lines) and corresponding coefficient of determination (R^2) are given for landslides grouped as blocky ($h_h/L_t > 0.01$) and disintegrative (($h_h/L_t < 0.01$). The landslides Bowl Slide (BS) and Gloria Knolls Slide (GKS) are also indicated.
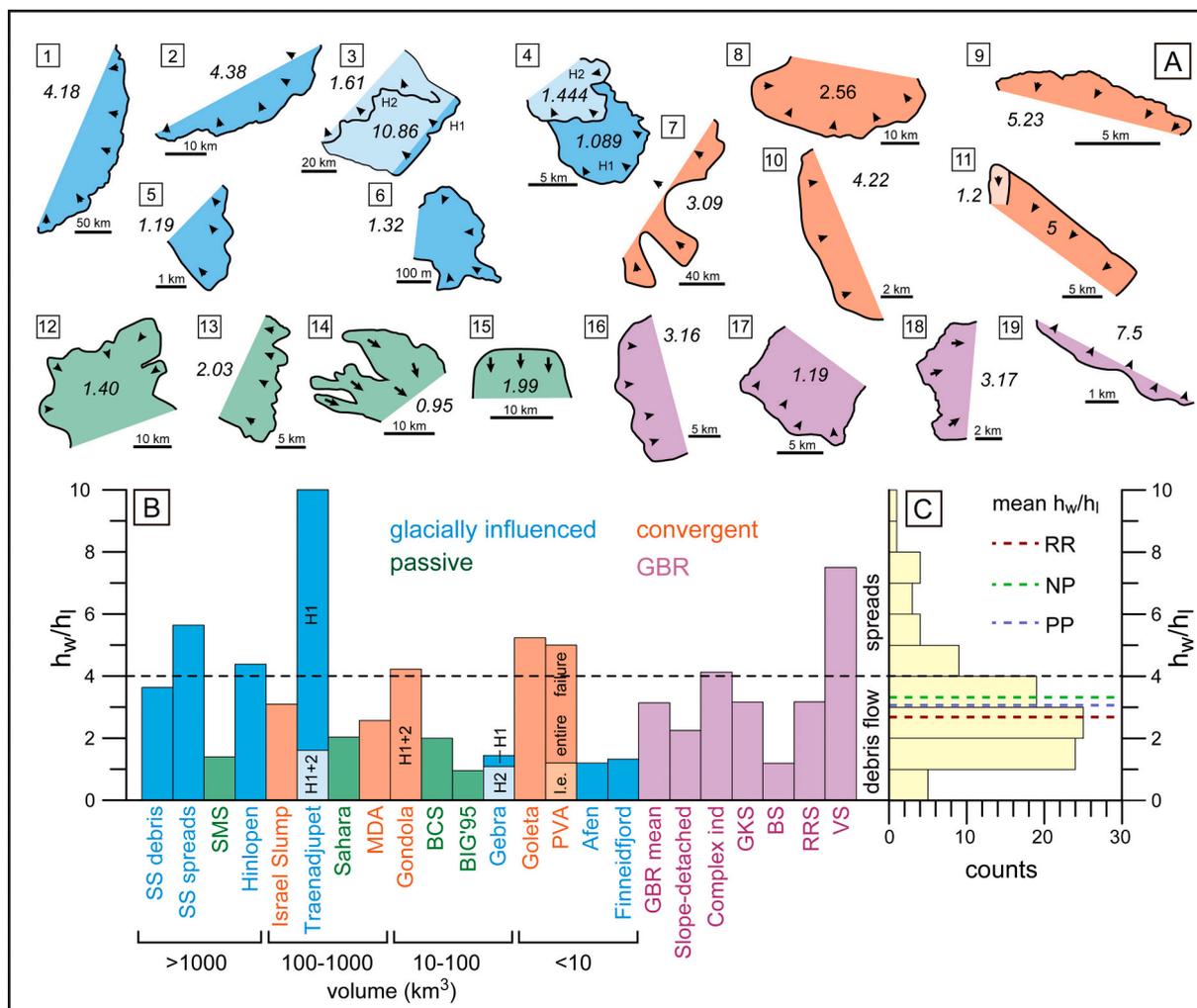
Fig. 14. A) Sketches showing the plan-view shape of the landslide headscarps from some representative landslides in the GBR margin and other selected landslides from different tectonic settings and varying sizes. Arrowheads point to the direction of evacuation. Numbers in italics corresponds to the value of the headscarp width/headscarp length ratio (h_w/h_l) also shown in B). 1: Storegga Slide; 2: Hinlopen Slide; 3: Traenadjupet Slide (H1 and H2 are the main headscarps in this landslide); 4: Gebra Slide; 5: Afen Slide; 6: Finneidfjord Slide; 7: Israel Slump; 8: Matakaoa Debris Avalanche (MDA); 9: Goleta Slide; 10: Gondola Slide (H1 and H2 are the main headscarps); 11: Palos Verdes Debris Avalanche (PVA) (both the entire landslide complex and the last event (l.e.) are shown); 12: South Makassar Strait Slide; 13: Sahara Slide; 14: BIG'95; 15: Block Composite Submarine landslide (BCS): 16: Gloria Knolls Slide (GKS); 17: Bowl Slide (BS); 18: Ribbon Reef Slide (RRS); 19: Viper Slide (VS). RRS: Ribbon Reef Slide; GKS: Gloria Knolls Slide; BS: Bowl Slide; VS: Viper Slide. Data compiled and redrawn from (compiled from Imbo et al., 2003; Longva et al., 2003; Bohannon and Gardner, 2004; Canals et al., 2004; Lastras et al., 2004a; Normark et al., 2004; Wilson et al., 2004; Frey-Martínez et al., 2005; Greene et al., 2006; Vanneste et al., 2006; Lamarche et al., 2008; Micallef et al., 2008; Georgiopoulou et al., 2010, Locat et al., 2010; Casas et al., 2013; Armandita et al., 2015; Dalla Valle et al., 2015; Allin, 2016; Webster et al., 2016; Li et al., 2017; Puga-Bernabéu et al., 2020). B) Vertical histogram showing the h_w/h_l values for landslides represented in A). The mean h_w/h_l value for the GBR landslides and the value for the subset of slope-detached landslides and individual landslides within complexes are also shown. The h_w/h_l ratio is indicative of the principal formative processes of the headscarps (Micallef et al., 2008). $h_w/h_l < 4$ suggests formation by debris flow while ratios >4 are indicative of spreads. C) Horizontal histogram showing the shape of the GBR landslide headscarps given by h_w/h_l and the mean value of this ratio in the study regions. RR: Ribbon Reef; NP: Noggin Passage; PP: Palm Passage.

example, downslope flow transformation into debris flow or turbidity currents, such as in the Storegga, Canary, Hinlopen or BIG'95 slides, adds significant distance to the total runout (e.g., 400 km in the Storegga Slide or about 90 km in the BIG'95; Canals et al., 2004; Haflidason et al., 2004). In the case of the BIG'95, which shows similarities to the GKS in terms of size and the morphology of the depositional area (Puga-Bernabéu et al., 2017), it has similar L_t-V ratios to the GBR landslides after discounting the runout distance corresponding to the debris flow part of the landslide (Fig. 16A). Other processes that favour extreme runout distances and deviation from the GBR trends are related to hydroplaning and fluidization, or with the presence of basal layers with low apparent friction characteristics (e.g., Hinlopen or Sahara Slide; Vanneste et al., 2006; Gee et al., 1999; Georgiopoulou et al., 2010).

Although both approaches (H/L-V and L_t-V) do not fully explain the

mobility of all natural landslides, as they do not take into account the intertwined role of volume and topography (Staron and Lajeunesse, 2009; Pudasaini and Miller, 2013), we propose they can be used together to infer the sedimentary processes and/or predict the runout length of submarine slope failures. Elverhøi et al. (2002) suggested that there is a threshold or "break point" that marks an increase in runout as a function of volume. For volumes below such a break, they proposed that the rheology of the mass controls the flow behaviour. Above the break point, the flow would increase its velocity and could potentially reach the critical value required to initiate hydroplaning. Elverhøi et al. (2002) proposed the volume of 1 km³ as the break point in flow behaviour, which is consistent with our dataset (Supplementary data 5-2). However, the threshold of the breaking point seems to be variable from one tectonic setting to another and within different datasets, normally
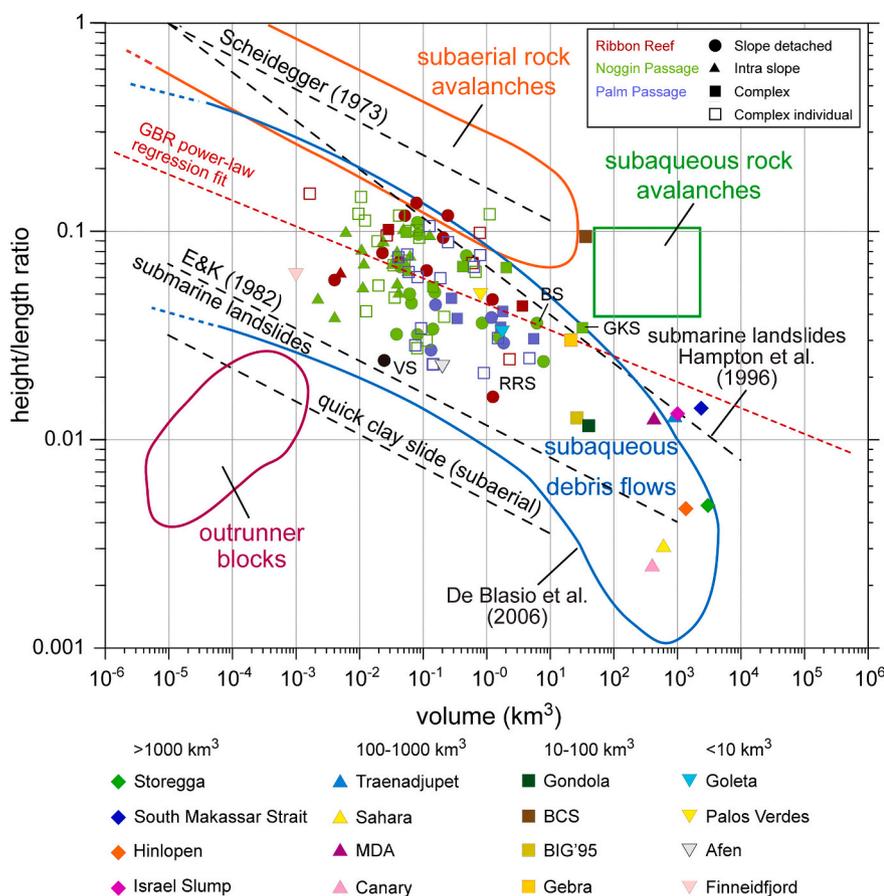
Fig. 15. Log-log plot showing the mobility of submarine and subaerial mass movements as a function of the height-length ratio versus volume of failed mass applied to the GBR landslides and comparison with other well-known mass transport deposits from different tectonic settings and varying sizes (compiled from Locat et al., 2004; Canals et al., 2004; Normark et al., 2004; Frey-Martínez et al., 2005; Greene et al., 2006; Vanneste et al., 2006; Lamarche et al., 2008; Georgiopoulou et al., 2010, Locat et al., 2010; Armandita et al., 2015; Dalla Valle et al., 2015). Curves from lower bound values for submarine landslides (E&K; Edgers and Karlsrud, 1982), subaerial quick clay slides (Edgers and Karlsrud, 1982), average values for subaerial landslides proposed by Scheidegger (1973), and upper bound for submarine landslides from Hampton et al. (1996) are plotted for reference. The coloured envelopes are from De Blasio et al. (2006). The dashed red line corresponds to the power-law regression fit for the GBR landslides. RRS: Ribbon Reef Slide; GKS: Gloria Knolls Slide; BS: Bowl Slide; VS: Viper Slide (Webster et al., 2016); MDA: Matakaoa Debris Avalanche; BCS: Block Composite Submarine landslide.

ranging from 1 to 10 km^3. Once the break point is identified, the plot H/L-V can be used to discern the potential landslide "hypermobility" (by hydroplaning or flow transformation). The boundary of H/L = 0.02 is suggested, based on the GBR dataset and by Elverhøi et al. (2002). Below this value, landslides may experience hypermobility. According to this assumption, the Ribbon Reef Slide (Puga-Bernabéu et al., 2020) is the only landslide in the GBR margin that may have experienced hydroplaning, which supports the idea of the relative low mobility of the GBR landslides. This conclusion is based on the analysis of a limited number of data points (at global scale), and therefore, needs to be confirmed by the comparison and integration of datasets from different margins worldwide.

5.1.3. Flow efficiency

Other important information that can be inferred from the morphometric analysis is the flow efficiency or a measurement of how the energy of a flow degrades before it stops. Issler et al. (2005) studied the flow efficiency of the different lobes that encompass the Storegga Slide by using the volume per unit width (here V/h$_w$). The GBR landslides fall above the best power-law fit to Storegga data for volumes <1 km^3 (Fig. 17A), indicating that they may have a higher efficiency per sediment volume released (per width unit). Our results are similar to those found by Moernaut and De Batist (2011) in landslides involving poorly-consolidated sublacustrine sediments. Therefore, a preliminary interpretation is that GBR slope failures likely involved relatively unconsolidated sediments compared with those comprising the Storegga Slide. However, larger lobes in the Storegga Slide (>1 km^3 volume per unit width) (Fig. 17A) seem to reach farther runout distances than the larger GBR landslides, which is consistent with their relatively low mobility inferred from the H/L-V relationship (Fig. 15) (see Section 5.2). Issler et al. (2005) proposed that, in general and in simplified terms,

visco-plastic models with fixed yield strengths reproduce the observed scaling behaviour if the failed mass is small. Therefore, the relationship L-V/h$_w$ could be used to infer the flow efficiency for small landslides within the same region. Very large masses would experience either change in flow regime or the sediment properties during their movement over the seafloor. However, the relationship between runout and volume per unit width has been unexplored even in very complete submarine landslide compilations (e.g., Urgeles and Camerlenghi, 2013; Moscardelli and Wood, 2016), and therefore its application and reliability is still to be compared with other datasets.

Dade and Huppert (1998) showed that the downslope spreading of large subaerial rockfalls and debris avalanches can be quantitatively described and evaluated by the ratio between the area and volume (A/V$^{2/3}$), where higher values reflect higher mass spreading efficiency (Gee et al., 2001, 2007; Haflidason et al., 2005; Armandita et al., 2015). The A/V$^{2/3}$ ratio of the GBR landslides is relatively low (the value of the median landslide is 51) compared with other landslides from different settings and varying dimensions (Fig. 17B). The largest GBR landslide, the GKS, has an A/V$^{2/3}$ ratio of 57 and only a few landslides have relatively high efficiency such as the Bowl Slide, Ribbon Reef Slide and Viper Slide, with A/V$^{2/3}$ values >100 (Fig. 17B) (Webster et al., 2016; Puga-Bernabéu et al., 2020).

The landslide volume does not directly control the spreading efficiency of the flows as comparable values of A/V$^{2/3}$ are shared by landslides with volumes that vary over 1 or 2 orders of magnitude (Fig. 17). The lithology of the failed mass is proposed as one of the main controlling factors on spreading efficiency (Ilstad et al., 2004; Elverhøi et al., 2010), but other factors, such as the seafloor topography and depth of the detachment surface, may explain the variation of A/V$^{2/3}$. The deep-rooted basal shear surface interpreted from the reconstructed slope in the GKS, together with small thrusts at the landslide toe that
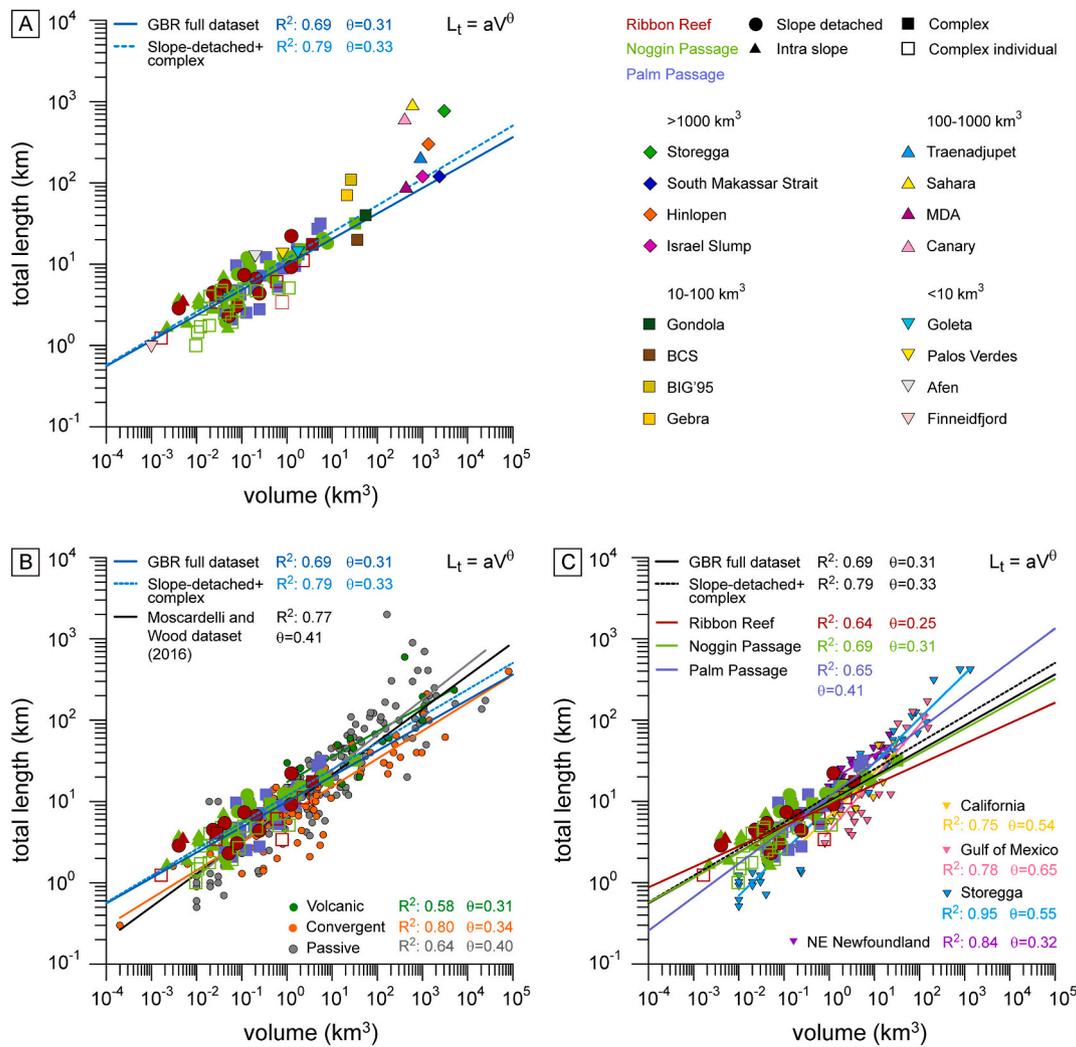
Fig. 16. Log-log plots showing the mobility of submarine mass movements as a function of the total length versus volume of failed mass applied to the GBR landslides. Coefficient of determination and scaling exponent (θ) to a power-law regression fit are given for each dataset. A) Comparison with other well-known landslides from different tectonic settings and varying sizes (same as in Fig. 15). B) Comparison with submarine mass movements from passive, convergent and volcanic margins (compiled from Moscardelli and Wood, 2016). C) Comparison with selected subsets of submarine mass movements from passive margins and the Storegga Slide (compiled from Moscardelli and Wood, 2016). Regression lines to a power-law fit and statistics from the study regions in the GBR margin are also shown.

may indicate some frontal confinement (Puga-Bernabéu et al., 2017), are consistent with low spreading efficiency of this large landslide. These features are comparable to those observed in the Israel Slump (A/$V^{2/3}$ = 48) and the South Makassar Strait Slide (A/$V^{2/3}$ = 51) (Frey-Martínez et al., 2005; Armandita et al., 2015). In the case of the GKS, we suggest that abrupt breaks-in-gradient at the slope toe can also favour the rapid dissipation of the potential energy of the failed mass that decreases its spreading over the seafloor. Similar breaks-in-gradient are also observed in the slopes where the Palos Verdes Avalanche (A/$V^{2/3}$ = 58) originated (Normark et al., 2004). This interpretation is also consistent with the lowest A/$V^{2/3}$ for the median landslide in the RR region where the lower slope is very steep and changes abruptly to a flat basin (Puga-Bernabéu et al., 2011). In contrast, the median landslide on rather uniform slopes in the PP region has the highest A/$V^{2/3}$ value (60).

The RRS, BS, and the GKS originated in open slopes and did not experience topographic confinement, and have in common the presence of a well-developed debris field on the depositional area, but their spreading efficiency is quite different as the first two landslides have significantly higher A/$V^{2/3}$ ratios (Fig. 17B). Such differences may result from the rather uniform slopes overrun by the failed mass in the RRS and BS, and the relatively thin thickness of the failed section compared with

the GKS.

5.2. Landslide seafloor extension

The GBR margin lacks giant submarine landslides such as those in the North Atlantic, as the largest landslide, the GKS (32 km³), is two orders of magnitude smaller than, for example, the Storegga Slide (Haflidason et al., 2004; Puga-Bernabéu et al., 2017). At the global scale, it seems that the total sediment volume remobilized by slope failures may be largely related to the presence of very large fluvial systems over long time periods (e.g., Niger or Congo rivers) (Moscardelli and Wood, 2016), which are absent on the GBR margin. The Burdekin River is the largest river in the GBR margin (~130.000 km² catchment area; Alexander et al., 1999), which is relatively small compared, for example, with the Atlantic Niger and Congo rivers (>4 × 10⁶ km² catchment areas; Campbell, 2005; Bonne, 2014). However, in terms of failed slope areas and total extension over the seafloor including the basin, the percentage in the GBR (12.6% and 15.5% respectively; Table 1) is within the range of other passive margins such as the middle Atlantic (16%), Cape Hatteras (western North Atlantic) (13%) and New Jersey margins (9.5%) (McAdoo et al., 2000; Twichell et al., 2009), is slightly higher than in
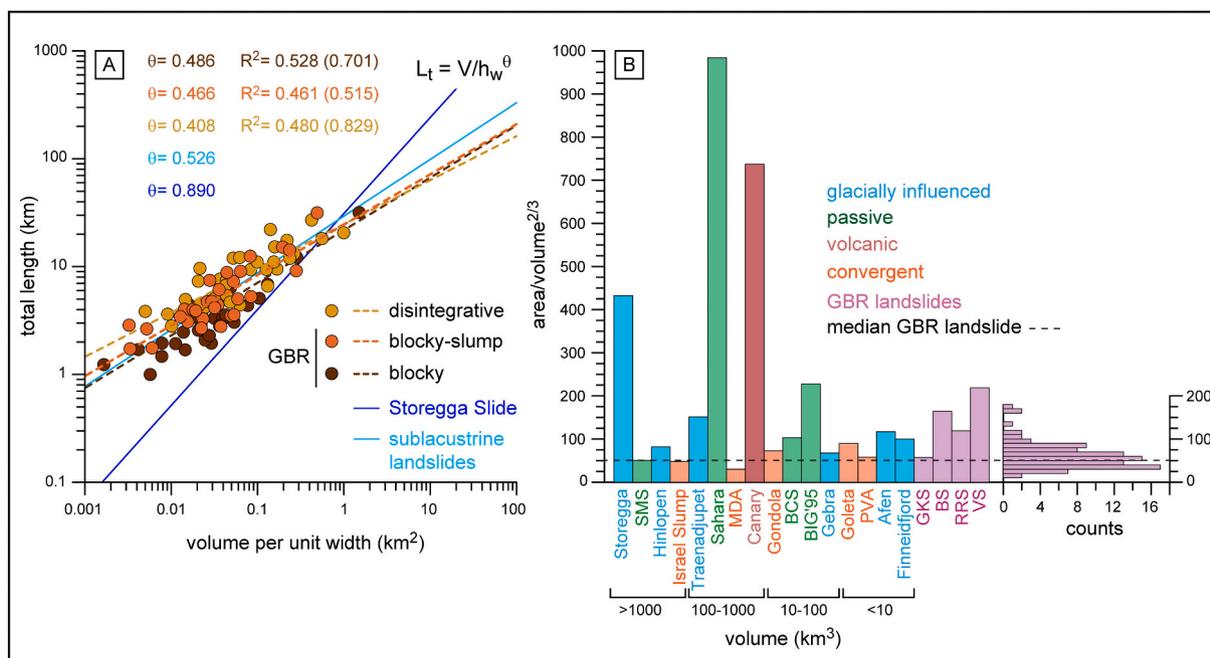
Fig. 17. Flow efficiency of submarine slope failures inferred from morphometric parameters and ratios. A) Log-log plot of the total length vs volume per unit width (V/h_w) for GBR landslides separated by disintegrative and blocky types as shown in Fig. 10. Statistics (coefficient of determination and scaling exponent to a power-law regression fit) for GBR landslides, Storegga Slide lobes (Issler et al., 2005) and sublacustrine landslides (Moernaut and De Batist, 2011) are also shown. B) Histogram of the $A/V^{2/3}$ ratio for the GBR landslides and selected landslides from different tectonic settings and varying sizes (the same as in Fig. 15).

active margins (e.g., 3–7% in the eastern U.S. Pacific margin and central Chile margin) (McAdoo et al., 2000; Völker et al., 2016), and is close to values in semi-enclosed seas such as the Mediterranean Sea (18%) (Urgeles and Camerlenghi, 2013), where different tectonic settings are represented. Therefore, submarine landslides are equally significant in the shaping of the GBR margin but with less sediment remobilization. It is also worth noting that the relationship between the slope margin area covered by scars and the average sedimentation rates on the margin (20–50 cm/ky; see Section 5.5), and between the area covered by scars and mean margin slope gradient, is consistent with the observations of ten Brink et al. (2016) for margins where slope failures seem to be related with earthquake frequency.

5.3. Frequency distributions

The landslide frequency–dimension statistics is one of the basic parameters used to characterize the inventories of these events regardless of their environment (subaerial, submarine or sublacustrine) (Malamud et al., 2004; Casas et al., 2016; Moernaut and De Batist, 2011). The scaling parameters for the different fitting distributions can be used to compare landslide inventories of different regions and discern common controls on the distributions or different failure processes (ten Brink et al., 2006; Moernaut and De Batist, 2011). The regression line exponents from the least squares method (θ_{LS}) and NLS (θ_{NLS}) of the power-law function for GBR landslide volume ($\theta_{LS} = 0.55$, $\theta_{NLS} = 0.47$) (Table 4) are within the range of exponents in landslides of different settings, such as the Storegga Slide ($\theta_{LS} = 0.44$; ten Brink et al., 2006), the Mediterranean Sea ($\theta_{NLS} = 0.54$ for the entire region, $\theta_{NLS} = 0.49$–0.55 for passive margins within the Mediterranean Sea; Urgeles and Camerlenghi, 2013), the George Bank ($\theta_{LS} = 0.62$) and Northern Baltimore Canyon Trough ($\theta_{LS} = 0.48$) areas of the US Atlantic margin (Chaytor et al., 2009), the carbonate cemented slopes of Puerto Rico ($\theta_{LS} = 0.64$; ten Brink et al., 2006), and sublacustrine landslides ($\theta_{LS} = 0.46$; Moernaut and De Batist, 2011). All these exponents are clearly <1, which means that the contribution to sediment remobilization is mostly due to a few large landslides within each region or dataset, but

independent of the landslide volume range for the fitting. For example, θ exponents are similar in the GBR, the Mediterranean Sea and for sublacustrine landslides ($\theta = 0.46$–0.55) regardless of the volume range covered by the power-law fitting (10^{-4}–1 km^3 for sublacustrine landslides (Moernaut and De Batist, 2011), 0.03–32 km^3 in the GBR margin, or 1–23,000 km^3 in the Mediterranean Sea (Urgeles and Camerlenghi, 2013)). These exponent values are also within the common range of subaerial rockfalls for time intervals commonly of less than 100 years ($\theta = 0.40$–0.46; Hungr et al., 1999; Dussauge et al., 2003) and worldwide rockslides ($\theta = 0.51$; Dussauge et al., 2003). However, θ exponents corresponding to subaerial rainfall-induced and surficial landslides are slightly higher ($\theta = 0.79$–0.87; Fujii, 1969; Dai and Lee, 2001; Martin et al., 2002). Higher θ values in subaerial landslides may result from different failure mechanisms, usually depending on the soil moisture and rainfall distribution, while submarine landslides and subaerial rockfalls may share common failure dynamics in terms of volume distribution. At the local scale, it has been suggested that higher θ values (e. g., $\theta = 0.65$–72) in some rockfall volume-frequency distributions may obey to local distribution (spacing) of joint and fault planes that may control the initial size of the blocks (Hungr et al., 1999). By analogy, within the submarine environment, larger θ exponents in the cemented carbonate slopes of Puerto Rico compared with the GBR margin and other datasets, could suggest some sort of structural control when failures involve well-consolidated material as in the case of Puerto Rico (ten Brink et al., 2006). Besides, small exponent values in the GBR margin suggest that relatively thin slope sections were affected during each event.

Similarly, some provisional comparisons can be made using scaling parameters from probability functions of volume distribution, bearing in mind that scaling parameters might have been obtained by different methods. The GBR margin scaling exponents (α, mean of 1.49) are consistent with unconsolidated slope failed sediments, as low ($\alpha < 1$) scaling exponents may involve consolidated or cemented slopes (ten Brink et al., 2006; Chaytor et al., 2009) The GBR margin scaling is similar to the values of $\alpha = 1.51$ found by Casas et al. (2016) for open slope landslides in the Tyrrhenian Sea.

In contrast to volume, the scaling exponents (both θ_{LS} and θ_{NLS}) of the power-law function for the cumulative-frequency landslide area in the GBR differ substantially from subaerial landslides. Subaerial failures commonly show θ exponents >1 (1.34–1.62, Ohmori and Hirano, 1988; 1.6–2.0, Pelletier et al., 1997; 1.3–1.5; Guzzetti et al., 2002; 1.56, Guthrie and Evans, 2004), while θ exponents in the GBR margin are ~1 for the full dataset ($\theta_{NLS} = 0.96$, $\theta_{LS} = 1.02$) or <1 in most of the subsets (e.g., θ exponents for frequency distribution in the study regions range between 0.5 and 0.77) (Fig. 11; Table 5). Therefore, the seafloor area affected and covered by landslides in the GBR is mostly due to relatively few large landslides. Comparison with other continental margins is difficult due to the scarce datasets available and the lack of published scaling parameters. Our data show that θ exponents are somehow comparable to the values of 0.52 ($\beta = 1.52$ for the non-cumulative frequency distribution) found in the mass movements from within the Storegga Slide scar (Micallef et al., 2008), 0.7 in the Israeli continental slope (Katz et al., 2015) or 0.80 for the landslides in the Mediterranean Sea (Urgeles and Camerlenghi, 2013). Slightly higher θ values in the case of the GBR may respond to the different type of datasets, i.e., individual landslides within a large region in our case and a single, large landslide complex in the Storegga Slide, or different tectonic settings included in the case of the Mediterranean Sea. We note that higher θ values for the full dataset may be biased due to the small number of landslides fitted with statistical significance, and thus, be representative only of the larger landslides (>42.4 km^2) in the distribution tail.

In the GBR, the total length landslide frequency cannot be statistically explained by a power-law distribution and it is better explained by an exponential distribution (Fig. 11; Table 6). This means that the frequency length of the GBR landslides is not scale invariant or self-similar, as suggested for the frequency landslide area (Micallef et al., 2008), and has a characteristic scale (i.e., the range over which the length changes by $1/e$). As with the area, comparison with other datasets of the cumulative-frequency of the total landslide length is equally difficult as, to our knowledge, only Moernaut and De Batist (2011) have provided scaling parameters (of a power-law function) for this parameter. Therefore, it is clearly desirable to obtain more landslide inventories to explore the geological meaning of the frequency–dimension (volume, area and total length) of submarine landslides.

5.3.1. Power-law vs log-normal frequency distributions

Submarine landslide size (area and volume) distribution commonly obeys a negative power law with a rollover in the smaller size. It is still a matter of debate whether such rollover corresponds to an artifact in the measurements due to the spatial resolution of the datasets or whether such distribution responds to geological controls at the site (Chaytor et al., 2009; Urgeles and Camerlenghi, 2013; Casas et al., 2016). We consider that the divergence from the power law cannot be necessarily attributed to the incompleteness of an inventory. For example, the cumulative probability distribution of landslide volume in the GBR is very similar to the distribution of smaller landslides in the Gioia Basin (Tyrrhenian Sea, Mediterranean Sea) (Casas et al., 2016) despite them covering four orders of magnitude less than the size of the smallest GBR landslide (Fig. 12). A possible explanation for the rollover in the size distribution (of subaerial landslides) has been recently proposed by Tanyas et al. (2019). These authors argue that smaller landslides can be undetectable because of reworking during a larger coalescent event including multiple landslides (for example during the upslope expansion of the landslide), and therefore, the number of mapped small landslides would always be less than the original. Additionally, the size of larger landslides could be overestimated because the mapping of such landslides may just be a snapshot of the geometry of an accumulation of successive sliding events. Such a snapshot of the seafloor bathymetry may include previous smaller landslides that are merged into the larger ones.

Another alternative to the additive avalanche process that involves the inverse power-law distribution of landslide size, is to consider that

the size of slope failures is predictable and depends on the magnitude of the trigger earthquake, i.e., the landslide size in a particular margin follows a lognormal distribution (Chaytor et al., 2009; ten Brink et al., 2009a). In this case, slope failures occur simultaneously over the area affected by horizontal ground shaking, and does not cascade from nucleating points as in the inverse power-law distribution (ten Brink et al., 2009a). On the GBR margin, in most cases, the power-law and lognormal distributions are statistically similar. In the case of the lognormal distribution, fitting is excellent within the full dataset of landslide volume, area and length (Fig. 11). Function parameters of the lognormal distribution ($\mu = 2.58$, $\sigma = 1.45$ for the landslide area) are similar to those found in the U.S. Atlantic margin ($\mu = 2.84$, $\sigma = 1.51$), despite the lognormal distribution being more characteristic of siliciclastic margins than carbonate or mixed margins (Geist and ten Brink, 2019). This suggests similar interseismic sediment accumulation between the two margins (ten Brink et al., 2016) yet there is a different sediment composition. The predicted value of total failed area ($A = n \exp(\mu + \sigma^2/2) = 3172 \text{ km}^2$) following a lognormal distribution is slightly lower (~7%) than the observed value of 2938 km^2 (Table 1). This estimation agrees with a lognormal size distribution, which likely reflects the minimum earthquake size capable of causing ground failures (Geist and ten Brink, 2019). On the GBR margin, mean slope gradients (<4°) (Table 2) and slope stability analysis (Puga-Bernabéu et al., 2013a) are consistent with the findings of ten Brink et al. (2009b) on the U.S. Atlantic margin. ten Brink et al. (2009b) showed that submarine slope failures are not expected to occur at earthquakes magnitudes <4.5–5 and at slope angles <6°.

We cannot conclude whether submarine landslide size on the GBR margin follows an inverse power-law or a lognormal distribution, and comparison with other margins is limited by the scarcity of available examples, especially for the lognormal distribution. It seems that the predictive lognormal function better explains the distribution from small to relatively large sizes without any rollover. An additive process (inverse power law) occurs at larger sizes, although the size of these larger events may be slightly overestimated during the landslide mapping by the incorporation of smaller events. In any case, these general size distributions are locally controlled by variation in the slope angle (e.g., different regions along the GBR margin), material strength (e.g., carbonate vs siliciclastic sediment in the slope sedimentary sequences), pore pressure (e.g., Section 5.2), etc. (ten Brink et al., 2009a).

5.4. Volume-area relationship

The relationship between landslide volume and area usually shows a good correlation coefficient ($R^2 > 0.8$) to a power-law function ($V = aA^\theta$) when both parameters are represented in a log-log plot (Fig. 9.1; Supplementary data 7-1). The corresponding regression line can be used as a predictive tool, for example, to estimate landslide volume from area, as volume can be difficult to assess from bathymetric or seismic datasets (Moscardelli and Wood, 2016). However, the scaling parameter (θ) of the volume-area relationship has also been suggested to depend on the geological characteristics of the margin (e.g., overpressure, lithology) and the failure processes (Chaytor et al., 2009).

The θ value of 1.272 for the GBR margin is higher than the Storegga Slide ($\theta = 1.032$) (ten Brink et al., 2006) and the global dataset studied by Moscardelli and Wood (2016) ($\theta = 1.112$). This suggests that on the GBR margin, relatively thicker sections of slope sediment failed during each event as volume does not increase linearly with the area ($\theta \sim 1$) as in the Storegga Slide and the global dataset. Especially relevant is that the volume-area relationship in the GBR is closer to active margins than to other passive margins. A subset of landslides in passive margins extracted from Moscardelli and Wood (2016) generates θ exponents of <1.08. In contrast, the subset of landslides on the convergent margins in the global dataset yields θ exponent of 1.278. This similarity to convergent margins is also supported by the high θ values (1.369) found in the Tyrrhenian Sea by Casas et al. (2016), although this dataset also

includes landslides within submarine canyons.

Urgeles and Camerlenghi (2013) found different scaling exponents for different failure types in the Mediterranean Sea. Debris avalanches, which is a common type on the GBR margin (Puga-Bernabéu et al., 2020), yield comparable power-law exponents (θ = 1.30) to our study dataset and is significantly different from slides, and also significantly different from the values of slides and glides (1.469). In sublacustrine environments, high power-law exponents (1.241–1.330) may respond to their morphological confinement (Moernaut and De Batist, 2011), which is not the common scenario for open slope submarine landslides. On the GBR margin, the depth of the basin could have limited the extension of the failed slope sediments over the seafloor as suggested by the good relationship between the depth at origin and the depth at termination of the landslides (Fig. 10-4; Table 3).

5.5. Margin physiography, preconditioning factors and triggering mechanisms

Constraining the morphometric characteristics and spatial distribution of submarine landslides is a first step towards understanding the physical processes that lead to these slope failures (Hill et al., 2017). Previous morphometric studies based on compilations of submarine landslides from different regions and global datasets have observed differences between tectonic settings and along continental margins (McAdoo et al., 2000; Twichell et al., 2009; Urgeles and Camerlenghi, 2013; Moscardelli and Wood, 2016). Along the GBR margin, there are marked physiographic variations (Puga-Bernabéu et al., 2013b) that influence the type and distribution of submarine landslides in three key aspects. First, the margin deepens and the slope steepens from south to north (PP to RR regions). Therefore, the depth distribution of the landslides is primarily controlled by their latitudinal position (Fig. 10). Second, the available sediment on the slope (normally unconsolidated) prone to failure is higher in the NP and PP regions compared with the RR region. This is consistent with the higher percentage of slope area affected by failures in the PP and NP regions (Figs. 2, 3 and 4; Table 1). Third, the density, size and area covered by submarine canyons increase from south to north (Table 1) (Puga-Bernabéu et al., 2011, 2013b). This explains the lack of intra-slope landslides in this region as there are relatively small slope areas between canyons. In the RR region, larger landslides are generated at deeper waters where the canyon-covered areas are smaller (Fig. 10). The scarcity of canyons in the PP region favours a more continuous slope area prone to fail that results in larger median landslide area and volume in this region (Supplementary data 2). This is consistent with interpretations by Masson et al. (2010), suggesting that areas of continental slope cut by canyons and those affected by large-scale slope failures are largely mutually exclusive.

In the GBR margin, sedimentation rates have varied at different time scales during the Late Quaternary and Holocene. At time frames <30 ka, the sedimentation rate on the slope between 200 m and 1000 m water depth is relatively moderate (20–50 cm/ky), but it is not uniform through time (Dunbar et al., 2000). Higher sedimentation rates occurred during the last transgression (6.5–14.7 ka) (19–42 cm/ky) and modern highstand (0–6 ka) (20–55 cm/ky) compared with the lowstand (14.7–31 ka) (2–6 cm/ky). Thus, these contrasting values could induce pore pressure differences in the uppermost sediment pile. Over longer periods (<1.5 Ma), sedimentation rates estimated from long ODP sediment cores in the slope transect through Sites 819–821 (Fig. 1) vary over an order of magnitude from moderate to high average rates (18 to 143 cm/ky) (Feary et al., 1993). Interestingly, sedimentary units with higher sedimentation rates occur at depths below the seafloor (Supplementary data 10) where eventual overpressured pore fluids could be driven laterally close to the base of the slope. There, the overburden stress is lower, and consequently, could favour slope failures as suggested for the New Jersey Continental slope (Dugan and Flemings, 2000) or the Storegga Slide (Masson et al., 2010).

High sedimentation rates and the presence of so-called weak layers in

the sedimentary sequences may pre-condition the continental margin slopes to fail (Kvalstad et al., 2005; Gatter et al., 2021). Puga-Bernabéu et al. (2017, 2020) suggested that on the mixed carbonate-siliciclastic GBR margin, the succession of layers with different properties, such as lithology, porosity and texture, could play an important role on where basal failure surfaces are localized. Some detachment surfaces of buried landslides show basal surfaces that correlate with the boundaries between Late Pleistocene multimetre-scale, coarsening upward cycles with varying proportions of carbonates and siliciclastics, from clay-rich sediments with numerous silt intercalations to carbonate-rich bioclastic wackestones (Davies et al., 1991; Glenn et al., 1993). The bulk modulus in the GBR clay-rich carbonate sediments is almost 4.5 times higher than in the clay-free carbonate sediments (the larger the increase in the bulk modulus, the softer is the sediment and higher is the pore pressure) (Chen et al., 1993). Therefore, some of these layers could potentially develop pore overpressures that weaken the slope so that other mechanisms, such as earthquakes, could cause the failure (see Puga-Bernabéu et al., 2013a for details). Local signs of pore overpressure are found at Ocean Drilling Program Leg 133 Site 819 (565 m water depth). There, Ladd et al. (1993) found underconsolidated micritic clayey chalks at 345 mbsf with overconsolidation ratios as low as 0.04.

Margin stratigraphic architecture can also control the localization of excess pore pressures built up at depth by inducing flow focusing at the base of slope (Dugan and Flemings, 2000; Hill et al., 2017). On the GBR margin, there is a change in the margin slope internal architecture from obliquely progradational to aggradational (Supplementary data 10) (Davies et al., 1991; Feary et al., 1993). Progradational sequences (seismic sequences 5–9) yield the highest sedimentation rates and are separated from the overlying aggradational sequences (seismic sequences 1–3) by the transitional seismic sequence 4, and the top of sequence 5 corresponds to a pronounced seismic discontinuity (Feary et al., 1993). Additionally, the change from progradational to aggradational sequences is accompanied by a change in the sedimentary facies (Davies et al., 1991; Feary et al., 1993). Interestingly, the transitional and aggradational sequences have been severely disrupted by slumping in the distal parts of the slope (Feary et al., 1993), suggesting that slope failures were concentrated immediately on top of the prograding clinoforms. Thus, localized differences in slope morphology resulting from regional unconformities could drive the slope to potentially fail. Cross-cutting relationships between reflectors suggest these buried slumps post-date sequence 4 (<930 ka) and are very likely <365 ka, as they affect mostly sequences 1 and 3. The varying slope physiography (e.g., Hill et al., 2017) could also be important in the generation of submarine landslides on the GBR margin. The low-gradient, mostly sigmoidal slopes in the NP and PP regions are affected by abundant open slope landslides, in contrast to steeper and more canyon-covered adjacent areas in the RR region (Fig. 1; Table 1) (Puga-Bernabéu et al., 2013b). Canyons could create lateral escape route for high pore pressure by dissecting the margin sediments and thus defusing the potential for large-scale failures (Masson et al., 2010).

5.6. Predictive tool and implications for submarine landslide hazard and tsunami risk assessment in the Australia and the GBR margins

Moscardelli and Wood (2016) highlighted the promising use of the morphometric relationships between landslides parameters to predict the dimensions of these features in subsurface areas of limited and/or low-resolution data, as well as in outcrop analogues. However, despite the significant number (332) of mass-transport deposits used in the global dataset of Moscardelli and Wood (2016), there are only 25 (7.5%) in the southern hemisphere, only three are examples from the Australian margin, and none in large mixed carbonate-siliciclastic provinces (e.g., GBR margin, eastern Brazilian margin or New Caledonia margin). Therefore, the GBR margin landslide inventory reduces this gap in the global database. Future studies could then explore in detail the likely differences, for instance, between active and passive margins and/or

siliciclastic vs carbonate or mixed margins. Further, knowledge of the distribution and morphometry of landslides at the regional scale of north-eastern Australia will also help to predict the morphology of those landslides that are only partially mapped with high-resolution multibeam data, as is currently the case south of the PP region.

Submarine landslide inventories and their morphometric characterization are essential to assess landslide susceptibility and hazards (McAdoo and Watts, 2004; ten Brink et al., 2006; Geist and Parsons, 2010). At margin scale, the absence of high-resolution 2D and 3D seismic data (as on the GBR margin) that allow the precise measurement of some parameters, especially volume and thickness, makes landslide compilations based on high-resolution bathymetry a valuable tool in risk assessment. One of the most important offshore marine hazards in Australia is tsunamis. At least 47 events have been catalogued since AD1858, and there is a high probability that many events have gone unrecorded (Dominey-Howes, 2007). Tsunamis that may impact the Australian coastline are thought to be mostly generated by far-field earthquakes, especially those originated in the subduction zones along the northern and eastern boundaries of the Australian plate (Dominey-Howes, 2007; Davies and Griffin, 2018). However, along the eastern and north-eastern Australia margin, submarine landslides on the nearby continental slope, which could be triggered by local earthquakes, can also pose a tsunamigenic threat as predicted by numerical simulations (Puga-Bernabéu et al., 2013a, 2017, 2020; Webster et al., 2016; Clarke et al., 2019; Mollison et al., 2020). The probability of reaching large tsunamigenic slope failures in the GBR margin has the non-negligible probability of 4–6% (Fig. 12) and even the median landslide (0.081 km^3 and 50–55% of probability) may be potentially tsunamigenic under certain conditions (Webster et al., 2016). The existing Probabilistic Tsunami Hazard Assessment (PTHA) in Australia considers only distant earthquake-generated tsunamis (Davies and Griffin, 2018). Such an assessment would be significantly improved with the inclusion of local sources for tsunamis generated by submarine landslides. The GBR landslide dataset presented in this study represents the most comprehensive catalogue along the entire Australian margin, and therefore, provides a first step to update the PTHA, as well as to develop preliminary flooding hazard maps based on landslide-generated tsunami run up. Our morphometric characterization provides the essential parameters (e.g., depth, width, length, volume, slope gradient, etc.) to perform numerical simulations (Grilli et al., 2009; Iglesias et al., 2012; Schnyder et al., 2016; Webster et al., 2016; Puga-Bernabéu et al., 2020). For example, we found a good correlation between the depth at origin and depth at termination in the GBR margin (Fig. 10-4) that can be used to estimate the potential height of the landslides. The GBR landslide database also shows that the number of landslides is not evenly distributed along the margin, which may help to determine which sections of the coast are exposed to the highest tsunamigenic risk.

6. Conclusions

The first comprehensive inventory of submarine landslides on the Great Barrier Reef margin of north-eastern Australia includes the detailed morphometric analysis of 84 landslides extending along ~500 km of this mixed carbonate-siliciclastic margin. This inventory helps to improve the knowledge base in worldwide catalogues of representative examples of submarine landslides in this type of setting, and provides a robust morphometric framework that allows comparison with existing and future slope failure databases. The main conclusions from this study include:

(1) The failed slope area (12.6%) and total extension area (15.5%) of the submarine landslides is similar to other passive margins. Therefore, submarine landslides are equally significant in the shaping of the GBR margin, but with less sediment remobilization (~73 km^3). The GBR slope margin area covered by landslide scars

is consistent with the corresponding average sedimentation rates for margins where slope failures relate to earthquake frequency.

(2) Slope failures on the GBR margin involved relatively unconsolidated sediments. Slope disintegration by debris flows is the dominant process along the entire GBR margin. Their spreading efficiency and mobility is relatively low and only few landslides might have experienced hydroplaning.

(3) Margin stratigraphy, fluid overpressure at the base of the slope and detachment surfaces at the boundary of lithological cycles may have preconditioned the slope to fail.

(4) The cumulative frequency distribution of landslide dimensions can be statistically explained either by a power-law distribution with a scaling parameter ($\theta = 0.47$–0.55 for landslide volume), similar to other passive margins, or by a lognormal distribution with function parameters ($\mu = 2.58$, $\sigma = 1.45$ for the landslide area) similar to some siliciclastic margins.

(5) We provide the basic morphometric parameters that can be used to undertake numerical simulations on landslide-generated tsunamis. This will improve the accuracy of the existing Probabilistic Tsunami Hazard Assessment in Australia, which currently considers only distant earthquake-generated tsunamis. Additionally, the good correlation between the depth at origin and at termination for the GBR landslides, together the uneven landslide distribution along the margin, may help to determine which sections of the coast are exposed to the highest tsunamigenic risk.

Supplementary data to this article can be found online at https://doi.org/10.1016/j.geomorph.2022.108179.

References

Abbey, E., Webster, J.M., Beaman, J., 2011. Geomorphology of submerged reefs on the shelf edge of the Great Barrier Reef: the influence of oscillating Pleistocene Sea-levels. Mar. Geol. 288, 61–78.

Alberico, I., Budillon, F., Casalbore, D., Di Fiore, V., Iavarone, R., 2018. A critical review of potential tsunamigenic sources as first step towards the tsunami hazard assessment for the Napoli Gulf. Nat. Hazards 92, 43–76.

Alexander, I., Kroon, D., Thompson, R., 1993. Late Quaternary paleoenvironmental change on the northeast Australian margin as evidenced in oxygen isotope stratigraphy, mineral magnetism, and sedimentology. In: McKenzie, J.A., Davies, P. J., Palmer-Julson, A. (Eds.), Proceedings of the Ocean Drilling Program, Scientific Results, vol. 133, pp. 129–161.

Alexander, J., Fielding, C.R., Pocock, G.D., 1999. Flood behaviour of the Burdekin River, tropical north Queensland, Australia. In: Marriott, S.B., Alexander, J. (Eds.), Floodplains: Interdisciplinary Approaches, Geological Society, London, Special Publications, 163. The Geological Society of London, pp. 27–40.

Allin, J.R., 2016. The timing and frequency of large-volume submarine landslides and turbidity currents along the north-eastern Atlantic Margin, 221 p. University of Southampton. http://eprints.soton.ac.uk/id/eprint/407493.

Armandita, C., Morley, C.K., Rowell, P., 2015. Origin, structural geometry, and development of a giant coherent slide: the South Makassar Strait mass transport complex. Geosphere 11, 376–403.

Beaman, R.J., 2018. 3DGBR. High-resolution depth model for the Great Barrier Reef - 30 m. Data Available from. Geoscience Australia, Canberra, Australia. http://pid.geoscience.gov.au/dataset/115066.

Bohannon, R.G., Gardner, J.V., 2004. Submarine landslides of San Pedro Escarpment, southwest of Long Beach, California. Mar. Geol. 203, 261–268.

Bonne, K., 2014. Reconstruction of the evolution of the Niger River and implications for sediment supply to the Equatorial Atlantic margin of Africa during the Cretaceous and the Cenozoic). In: Scott, R.A., Smyth, H.R., Morton, A.X., Richarson, N. (Eds.), Sediment Provenance Studies in Hydrocarbon Exploration and Production, Geological Society, London, Special Publications, 386. The Geological Society of London, pp. 327–349.

Braithwaite, C.J.R., Dalmasso, H., Gilmour, M.A., Harkness, D.D., Henderson, G.M., Kay, R.L.F., Kroon, D., Montaggioni, L.F., Wilson, P.A., 2004. The Great Barrier Reef: the chronological record from a new borehole. J. Sediment. Res. 74, 298–310.

Calvès, G., Huuse, M., Clift, P.D., Brusset, S., 2015. Giant fossil mass wasting off the coast of West India: the Nataraja submarine slide. Earth Planet. Sci. Lett. 432, 265–272.

Campbell, D., 2005. The Congo River basin. In: Fraser, L., Keddy, P. (Eds.), The World's Largest Wetlands: Ecology and Conservation. Cambridge University Press, Cambridge, pp. 149–165.

Canals, M., Lastras, G., Urgeles, R., Casamor, J.L., Mienert, J., Cattaneo, A., De Batist, M., Haflidason, H., Imbo, Y., Laberg, J.S., Locat, J., Long, D., Longva, O., Masson, D.G., Sultan, N., Trincardi, F., Bryn, P., 2004. Slope failure dynamics and impacts from seafloor and shallow sub-seafloor geophysical data: case studies from the COSTA project. Mar. Geol. 213, 9–72.

Casalbore, D., Romagnoli, C., Bosman, A., Chiocci, F.L., 2011. Potential tsunamigenic landslides at Stromboli Volcano (Italy): Insight from marine DEM analysis. Geomorphology 126, 42–50.

Casalbore, D., Clementucci, R., Bosman, A., Chiocci, F.L., Martorelli, E., Ridente, D., 2020. Widespread mass-wasting processes off NE Sicily (Italy): insights from morpho-bathymetric analysis. Geol. Soc. Lond., Spec. Publ. 500, 393–403.

Casas, D., Ercilla, G., García, M., Yenes, M., Estrada, F., 2013. Post-rift sedimentary evolution of the Gebra Debris Valley. A submarine slope failure system in the Central Bransfield Basin (Antarctica). Mar. Geol. 340, 16–29.

Casas, D., Chiocci, F., Casalbore, D., Ercilla, G., Ortiz de Urbina, J., 2016. Magnitude-frequency distribution of submarine landslides in the Gioia Basin (southern Tyrrhenian Sea). Geo-Mar. Lett. 36, 405–414.

Chaytor, J.D., ten Brink, U.S., Slow, A.R., Andrews, B.D., 2009. Size distribution of submarine landslides along the U.S. Atlantic margin. Mar. Geol. 264, 16–27.

Chaytor, J.D., Demopoulos, A.W.J., ten Brink, U.S., Baxter, C., Quattrini, A.M., Brothers, D.S., 2016. Assessment of canyon wall failure process from multibeam bathymetry and remotely operated vehicle (ROV) observations, U.S. Atlantic Continental Margin. In: Lamarche, G., Mountjoy, J., Bull, S. (Eds.), Submarine Mass Movements and their Consequences, Advances in Natural and Technological Hazards Research, 41, pp. 103–113.

Chen, M.-P., Juang, J.-S., Ladd, J., 1993. Physical properties, compresional-wave velocity, and consolidation characteristics of slope sediments, Townsville Trough, NE Australia. In: McKenzie, J.A., Davies, P.J., Palmer-Julson, A. (Eds.), Proceedings of the Ocean Drilling Program, Scientific Results, 133, pp. 625–632.

Chiocci, F.L., Casalbore, D., 2017. Unexpected fast rate of morphological evolution of geologically-active continental margins during Quaternary: examples from selected areas in the italian seas. Mar. Pet. Geol. 82, 154–162.

Clarke, S.L., Hubble, T.C.T., Miao, G., Airey, D.W., Ward, S.N., 2019. Eastern Australia's submarine landslides: implications for tsunami hazard between Jervis Bay and Fraser Island. Landslides 16, 2059–2085.

Clauset, A., Shalizi, C.R., Newman, M.E.J., 2009. Power-law distributions in empirical data. SIAM Rev. 51, 661–703.

Dade, W.B., Huppert, H.E., 1998. Long-runout rockfalls. Geology 26, 803–806.

Dai, F.C., Lee, C.F., 2001. Frequency-volume relation and prediction of rainfall-induced landslides. Eng. Geol. 59, 253–266.

Dalla Valle, G., Gamberi, F., Foglini, F., Trincardi, F., 2015. The Gondola Slide: a mass transport complex controlled by margin topography (South-Western Adriatic margin, Mediterranean Sea). Mar. Geol. 366, 97–113.

Davies, T.R.H., 1982. Spreading of rock avalanche debris by mechanical fluidization. Rock Mech. 15, 9–24.

Davies, P.J., 2011. Great Barrier reef: origin, evolution, and modern development. In: Hopley, D. (Ed.), Encyclopedia of Modern Coral Reef: Structure, Form and Processes. Encyclopedia of Earth Sciences Series. Springer, Dordrecht. https://doi.org/10.1007/978-90-481-2639-2_88.

Davies, G., Griffin, J., 2018. The 2018 Australian probabilistic tsunami hazard assessment: hazard from earthquake generated tsunamis. Record 2018/41. Geoscience Australia, Canberra. https://doi.org/10.11636/Record.2018.041.

Davies, P.J., Symonds, P.A., Feary, D.A., Pigram, J., 1989. The evolution of the carbonate platforms of northeast Australia. In: Crevello, P.D., Wilson, J.L., Sarg, J.F., Read, J.F. (Eds.), Controls on Carbonate Platform and Basin Development, 44. SEPM Special Publication, pp. 233–258.

Davies, P.J., McKenzie, J.A., Palmer-Julson, A., et al., 1991. Proceedings of the Ocean Drilling Program Initial Reports 133. Ocean Drilling Program, College Station, TX. https://doi.org/10.2973/odp.proc.ir.133.1991.

De Blasio, F.V., Elverhøi, A., Engvik, L.E., Issler, D., Gauer, P., Harbitz, C., 2006. Understanding the high mobility of subaqueous debris flows. Nor. J. Geol. 86, 275–284.

Dominey-Howes, D., 2007. Geological and historical records of tsunami in Australia. Mar. Geol. 239, 99–123.

Dubois, N., Kindler, P., Spezzaferri, S., Coric, S., 2008. The initiation of the southern central Great Barrier Reef: new multiproxy data from Pleistocene distal sediments from the Marion Plateau (NE Australia). Mar. Geol. 250, 223–233.

Dugan, B., Flemings, P.B., 2000. Overpressure and fluid flow in the New Jersey continental slope: implications for slope failure and cold seeps. Science 289, 288–291.

Dunbar, G.B., Dickens, G.R., 2003a. Massive siliciclastic discharge to slopes of the Great Barrier Reef Platform during sea-level transgression: constraints from sediment cores between 15° and 16° latitude and possible explanations. Sediment. Geol. 162, 141–158.

Dunbar, G.B., Dickens, G.R., 2003b. Late Quaternary shedding of shallow-marine carbonate along a tropical mixed siliciclastic–carbonate shelf: Great Barrier Reef, Australia. Sedimentology 50, 1061–1077.

Dunbar, G.B., Dickens, G.R., Carter, R.M., 2000. Sediment flux across the Great Barrier Reef Shelf to the Queensland Trough over the last 300 ky. Sediment. Geol. 133, 49–92.

Dussaume, C., Grasso, J., Helmstetter, A., 2003. Statistical analysis of rockfall volume distributions: implication for rockfall dynamics. J. Geophys. Res. 108 (B6), 2286. https://doi.org/10.1029/2001JB000650.

Edgers, L., Karlsrud, K., 1982. Soil flows generated by submarine slides: case studies and consequences. In: Chryssostomomidis, C., Connor, J.J. (Eds.), Proceedings of the Third International Conference on the Behavior of Offshore Structures, vol. 2. Hemisphere Publications, Bristol, PA, pp. 425–437.

Elverhøi, A., De Blasio, F.V., Butt, F.A., Issler, D., Harbitz, C., Engvik, L., Solheim, A., Marr, J., 2002. Submarine mass-wasting on glacially-influenced continental slopes: processes and dynamics. In: Dowdeswell, J.A., Ò Cofaigh, C. (Eds.), Glacier-influenced Sedimentation on High-Latitude Continental Margins. Geological Society of London, Special Publications, 203. The Geological Society of London, pp. 73–87.

Elverhøi, A., Breien, H., De Blasio, F.V., Harbitz, C.B., Pagliardi, M., 2010. Submarine landslides and the importance of the initial sediment composition for run-out length and final deposit. Ocean Dyn. 60, 1027–1046.

Feary, D.A., Symonds, P.A., Davies, P.D., Pigram, C.J., Jarrard, R.D., 1993. Geometry of Pleistocene facies on the Great Barrier Reef outer shelf and upper slope–Seismic stratigraphy of Sites 819, 820 and 821. In: McKenzie, J.A., Davies, P.J., Palmer-Julson, A. (Eds.), Proceedings of the Ocean Drilling Program, Scientific Results, vol. 133, pp. 327–351.

Francis, J.M., Dunbar, G.B., Dickens, G.R., Sutherland, I.A., Droxler, A.W., 2007. Siliciclastic sediment across the North Queensland margin (Australia): a Holocene perspective on reciprocal versus coeval deposition in tropical mixed siliciclastic-carbonate systems. J. Sediment. Res. 77, 572–586.

Frey-Martínez, J., Cartwright, J., Hall, B., 2005. 3D seismic interpretation of slump complexes: examples from the continental margin of Israel. Basin Res. 17, 83–108.

Fujii, Y., 1969. Frequency distribution of the magnitude of the landslides caused by heavy rain-fall. Seismol. Soc. Jpn. J. 22, 244–247.

Gaina, C., Müller, R.D., Royer, J., Symonds, P., 1999. Evolution of the Louisiade triple junction. J. Geophys. Res. 104 (B6), 12927–12939.

Gatter, R., Clare, M.A., Kuhlmann, J., Huhn, K., 2021. Characterisation of weak layers, physical controls on their global distribution and their role in submarine landslide formation. Earth Sci. Rev. 223, 103845.

Gee, M.J.R., Masson, D.G., Watts, A.B., Allen, P.A., 1999. The Saharan debris flow: an insight into the mechanics of long runout submarine debris flows. Sedimentology 46, 317–335.

Gee, M.J.R., Watts, A.B., Masson, D.G., Mitchell, N.C., 2001. Landslides and the evolution of El Hierro in the Canary Islands. Mar. Geol. 177, 271–293.

Gee, M.J.R., Uy, H.D., Warren, J., Morley, C.K., Lambiase, J.J., 2007. The Brunei slide: a giant submarine landslide on the North West Borneo margin revealed by 3D seismic data. Mar. Geol. 246, 9–23.

Geist, E.L., Parsons, T., 2010. Estimating the empirical probability of submarine landslide occurrence. In: Mosher, D.C., et al. (Eds.), Submarine Mass Movements and Their Consequences, Advances in Natural and Technological Hazards Research, 28, pp. 377–386. https://doi.org/10.1007/978-90-481-3071-9_31.

Geist, E.L., ten Brink, U.S., 2019. Offshore landslide hazard curves from mapped landslide size distributions. J. Geophys. Res. Solid Earth 124, 3320–3334. https://doi.org/10.1029/2018JB017236.

Georgiopoulou, A., Masson, D.G., Wynn, R.B., Krastel, S., 2010. Sahara slide: age, initiation, and processes of a giant submarine slide. Geochem. Geophys. Geosyst. 11 (7), Q07014 https://doi.org/10.1029/2010GC003066.

Gillespie, C.S., 2015a. PoweRlaw: analysis of heavy tailed distributions. R package version 0.70.1. URL. http://CRAN.R-project.org/package=poweRlaw.

Gillespie, C.S., 2015b. Fitting heavy tailed distributions: the poweRlaw package. J. Stat. Softw. 64 (2) https://doi.org/10.18637/jss.v064.i02.

Glenn, C.R., Kroon, D., Wei, W., 1993. Sedimentary rhythms and climatic forcing of Pleistocene-Holocene mixed carbonate/siliciclastic sediments off the Great Barrier Reef. In: McKenzie, J.A., Davies, P.J., Palmer-Julson, A. (Eds.), Proceedings of the Ocean Drilling Program, Scientific Results, vol. 133, pp. 189–202.

Greene, H.G., Murai, L.Y., Watts, P., Maher, N.A., Fisher, M.A., Paull, C.E., Eichhubl, P., 2006. Submarine landslides in the Santa Barbara Channel as potential tsunami sources. Nat. Hazards Earth Syst. Sci. 6, 63–88.

Grilli, S.T., Taylor, O.-D.S., Baxter, C.D.P., Martzke, S., 2009. A probabilistic approach for determining submarine landslide tsunami hazard along the upper east coast of the United States. Mar. Geol. 264, 74–97.

Guthrie, R.H., Evans, S.G., 2004. Analysis of landslide frequencies and characteristics in a natural system, coastal British Columbia. Earth Surf. Process. Landf. 29, 1321–1339.

Guzzetti, F., Malamud, B.D., Turcotte, D.L., Reichenbach, P., 2002. Power-law correlations of landslide areas in Central Italy. Earth Planet. Sci. Lett. 195, 169–183.

Haflidason, H., Sejrup, H.P., Nygard, A., Mienert, J., Bryn, P., Lien, R., Forsberg, C.F., Berg, K., Masson, D., 2004. The Storegga Slide: architecture, geometry and slide development. Mar. Geol. 213, 201–234.

Haflidason, H., Lien, R., Sejrup, H.P., Forsberg, C.F., Bryn, P., 2005. The dating and morphometry of the Storegga Slide. Mar. Pet. Geol. 22, 123–136.

Hampton, M.A., Lee, H.J., Locat, J., 1996. Submarine landslides. Rev. Geophys. 34, 33–59. https://doi.org/10.1029/95RG03287.

Hill, K.C., Hall, R., 2003. Mesozoic-Cenozoic evolution of Australia's New Guinea margin in a west Pacific context. In: Hillis, R.R., Müller, R.D. (Eds.), Evolution and Dynamics of the Australian Plate, Special Papers – Geological Society of America, 372, pp. 265–290.

Hill, J.C., Brothers, D.S., Craig, B.K., ten Brink, U.S., Chaytor, J.D., Flores, C.H., 2017. Geologic controls on submarine slope failure along the central U.S. Atlantic margin: insights from the Currituck Slide complex. Mar. Geol. 385, 114–130.

Hühnerbach, V., Masson, D.G., partners of the COSTA-Project, 2004. Landslides in the North Atlantic and its adjacent seas: an analysis of their morphology, setting and behaviour. Mar. Geol. 213, 343–362.

Humblet, M., Webster, J.M., 2017. Coral community changes in the Great Barrier Reef in response to major environmental changes over glacial-interglacial timescales. Palaeogeogr. Palaeoclimatol. Palaeoecol. 472, 216–235.

Hungr, O., Evans, S.G., Hazzard, J., 1999. Magnitude and frequency of rock falls and rock slides along the main transportation corridors of southwestern British Columbia. Can. Geotech. J. 36, 224–238. https://doi.org/10.1139/t98-106.

Iglesias, O., Lastras, G., Canals, M., Olabarrieta, M., González, M., Aniel-Quiroga, I., Otero, L., Durán, R., Amblas, D., Casamor, J.L., Tahchi, E., Tinti, S., De Mol, B., 2012. The BIG'95 submarine landslide-generated tsunami: a numerical simulation. J. Geol. 120, 31–48.

Ilstad, T., Elverhøi, A., Issler, D., Marr, J.G., 2004. Subaqueous debris flow behaviour and its dependence on the sand/clay ratio: a laboratory study using particle tracking. Mar. Geol. 213, 415–438.

Imbo, Y., De Batist, M., Canals, M., Prieto, M.J., Baraza, J., 2003. The Gebra Slide: a submarine slide on the Trinity Peninsula margin, Antarctica. Mar. Geol. 193, 235–252.

Issler, D., De Blasio, F.V., Elverhøi, A., Bryn, P., Lien, R., 2005. Scaling behaviour of clay-rich submarine debris flows. Mar. Pet. Geol. 22, 187–194.

Jobe, Z.R., Howes, N., Romans, B.W., Covault, J.A., 2018. Volume and recurrence of submarine-fan-building turbidity currents. Depositional Rec. 4, 160–176.

Katz, O., Reuven, E., Aharonov, E., 2015. Submarine landslides and fault scarps along the eastern Mediterranean israeli continental-slope. Mar. Geol. 369, 100–115.

Kawamura, K., Laberg, J.S., Kanamatsu, T., 2014. Potential tsunamigenic submarine landslides in active margins. Mar. Geol. 356, 44–49.

Kershaw, A.P., van der Kaars, S., Moss, P.T., 2003. Late Quaternary Milankovitch-scale climatic change and variability and its impact on monsoonal Australasia. Mar. Geol. 201, 81–95.

Klar, A., Aharonov, E., Kalderon-Asael, B., Katz, O., 2011. Analytical and observational relations between landslide volume and surface area. J. Geophys. Res. 116, F02001 https://doi.org/10.1029/2009JF001604.

Kvalstad, T.J., Andressen, L., Forsberg, C.F., Berg, K., Bryn, P., Wangen, M., 2005. The Storegga slide: evaluation of triggering sources and slide mechanics. Mar. Pet. Geol. 22, 245–256.

Ladd, J., Moran, K., Kroon, D., Jarrard, R., Chen, M.-P., Palmer-Julson, A., Glenn, C., 1993. Porosity variation and consolidation on the northeastern Australian margin. In: McKenzie, J.A., Davies, P.J., Palmer-Julson, A. (Eds.), Proceedings of the Ocean Drilling Program, Scientific Results, 133, pp. 617–623.

Lamarche, G., Joanne, C., Collot, J.-Y., 2008. Successive, large mass-transport deposits in the south Kermadec fore-arc basin, New Zealand: the Matakaoa Submarine Instability complex. Geochem. Geophys. Geosyst. 9 (4), Q04001 https://doi.org/10.1029/2007GC001843.

Lastras, G., Canals, M., Urgeles, R., De Batist, M., Calafat, A.M., Casamar, J.L., 2004a. Characterisation of a recent debris flow deposit on the Ebro margin, Western Mediterranean Sea, after a variety of seismic reflection data. Mar. Geol. 231, 235–255.

Lastras, G., Canals, M., Urgeles, R., Hughes-Clarke, J.E., Acosta, J., 2004b. Shallow slides and pockmark swarms in the Eivissa Channel, western Mediterranean Sea. Sedimentology 51, 837–850.

Lawrence, K.T., Herbert, T.D., 2005. Late Quaternary Sea-surface temperatures in the western Coral Sea: implications for the growth of the Australian Great Barrier Reef. Geology 33, 677–680.

Lee, H.J., 2009. Timing of occurrence of large submarine landslides on the Atlantic Ocean margin. Mar. Geol. 265, 53–64.

Legros, F., 2002. The mobility of long-runout landslides. Eng. Geol. 63 (3-4), 301–331. https://doi.org/10.1016/S0013-7952(01)00090-4.

Li, W., Alves, T.M., Urlaub, M., Georgiopoulou, A., Klaucke, I., Wynn, R.B., Gross, F., Meyer, M., Respschläger, Berndt, C., Krastel, S., 2017. Morphology, age and sediment dynamics of the upper headwall of the Sahara Slide Complex, Northwest Africa: evidence for a large Late Holocene failure. Mar. Geol. 393, 109–123.

Locat, J., 2019. Failure and post-failure analysis of submarine mass movements using geomorphology and geomechanical concepts. In: Lintern, D.G., Mosher, D.C., Moscardelli, L.G. (Eds.), Subaqueous Mass Movements, 477. Geological Society, London, Special Publications, pp. 333–351.

Locat, J., Lee, H.J., Locat, P., Imran, J., 2004. Numerical analysis of the mobility of the Palos Verdes debris avalanche, California, and its implication for the generation of tsunamis. Mar. Geol. 204, 269–280.

Locat, J., ten Brink, U.S., Chaytor, J.D., 2010. The block composite submarine landslide, southern New England slope, U.S.A.: a morphological analysis. In: Mosher, D.C., Shipp, R.C., Moscardelli, L., Chaytor, J.D., Baxter, C.D.P., Lee, H.J., Urgeles, R. (Eds.), Submarine Mass Movements and Their Consequences: Advances in Natural and Technological Hazards Research, 28. Springer, The Netherlands, Dordrecht, pp. 267–277.

Longva, O., Janbu, N., Blikra, L.H., Boe, R., 2003. The 1996 Finneidfjord Slide, seafloor failure and slide dynamics. In: Locat, J., Mienert, J. (Eds.), Submarine Mass Movements and Their Consequences: Advances in Natural and Technological Hazards Research, 19. Kluwer Academic Publishers, Dordrecht, pp. 531–538.

Malamud, B.D., Turcotte, D.L., Guzzetti, F., Reichenbach, P., 2004. Landslide inventories and their statistical properties. Earth Surf. Process. Landf. 29, 687–711.

Martin, Y., Rood, K., Schwab, J.W., Church, M., 2002. Sediment transfer by shallow landsliding in the Queen Charlotte Islands, British Columbia. Can. J. Earth Sci. 39, 189–205.

Masson, D.G., Harbitz, C.B., Wynn, R.B., Pedersen, G., Løvholt, F., 2006. Submarine landslides: processes, triggers and hazard prediction. Philos. Trans. R. Soc. Acad. 364, 2009–2039.

Masson, D.G., Wynn, R.B., Talling, P.J., 2010. Large landslides on passive continental margins: processes, hypotheses and outstanding questions. In: Mosher, D.C., Shipp, R.C., Moscardelli, L., Chaytor, J.D., Baxter, C.D.P., Lee, H.J., Urgeles, R. (Eds.), Submarine Mass Movements and Their Consequences: Advances in Natural and Technological Hazards Research, 28. Springer, The Netherlands, Dordrecht, pp. 153–165.

McAdoo, B.G., Watts, P., 2004. Tsunami hazard from submarine landslides on the Oregon continental slope. Mar. Geol. 203, 235–245.

McAdoo, B.G., Pratson, L.F., Orange, D.L., 2000. Submarine landslide geomorphology, US continental slope. Mar. Geol. 169, 103–136.

Micallef, A., Berndt, C., Masson, D.G., Stow, A.V.D., 2008. Scale invariant characteristics of the Storegga Slide and implications for large-scale submarine mass movements. Mar. Geol. 247, 46–60.

Moernaut, J., De Batist, M., 2011. Frontal emplacement and mobility of sublacustrine landslides: results from morphometric and seismostratigraphic analysis. Mar. Geol. 285, 29–45.

Mollison, K.C., Power, H.E., Clarke, S.L., Baxter, A.T., Lane, E.M., Hubble, T.C.T., 2020. The sedimentology and tsunamigenic potential of the Byron submarine landslide off New South Wales, Australia. In: Georgiopoulou, A., Amy, L.A., Benetti, S., Chaytor, J.D., Clare, M.A., Gamboa, D., Haughton, P.D.W., Moernaut, J., Mountjoy, J.J. (Eds.), ous Mass Movements and their Consequences: Advances in Process Understanding, Monitoring and Hazard Assessments, 500. Geological Society, London, Special Publications, pp. 27–40.

Moscardelli, L., Wood, L., 2008. New classification system for mass transport complexes in offshore Trinidad. Basin Res. 20, 73–98. https://doi.org/10.1111/j.1365-2117.2007.00340.x.

Moscardelli, L., Wood, L., 2016. Morphometry of mass-transport deposits as a predictive tool. Geol. Soc. Am. Bull. 128, 47–80.

Nadim, F., 2006. Challenges to geo-scientists in risk assessment for submarine slides. Nor. J. Geol. 86, 351–362.

Nadim, F., Locat, J., 2005. Risk assessment for submarine slides. In: Hungr, O., Fell, R., Couture, R., Eberhardt, E. (Eds.), Landslides Risk Management. Taylor & Francis Group, London, pp. 331–334.

Normark, W.R., McGann, M., Sliter, R., 2004. Age of Palos Verdes submarine debris avalanche, southern California. Mar. Geol. 203, 247–259.

Ohmori, H., Hirano, M., 1988. Magnitude, frequency and geomorphological significance of rocky mud fows, landcreep and the collapse of steep slopes. Z. Geomorphol. Suppl. 67, 55–65.

Owen, M., Day, S., Maslin, M., 2007. Late Pleistocene submarine mass movements: occurrence and causes. Quat. Sci. Rev. 26, 958–978.

Page, M.C., Dickens, G.R., Dunbar, G.B., 2003. Tropical view of Quaternary sequence stratigraphy. Siliciclastic accumulation on slopes east of the Great Barrier Reef since the last Glacial Maximum. Geology 31, 1013–1016.

Pelletier, J.D., Malamud, B.D., Blodgett, T., Turcotte, D.L., 1997. Scale-invariance of soil moisture variability and its implications for the frequency-size distribution of landslides. Eng. Geol. 48, 255–268.

Prélat, A., Covault, J.A., Hodgson, D.M., Fildani, A., Flint, S.S., 2010. Intrinsic controls on the range of volumes, morphologies, and dimensions of submarine lobes. Sediment. Geol. 232, 66–76.

Pudasaini, S.P., Miller, S.A., 2013. The hypermobility of huge landslides and avalanches. Eng. Geol. 157, 124–132.

Puga-Bernabéu, Á., Webster, J.M., Beaman, R.J., Guilbaud, V., 2011. Morphology and controls on the evolution of a mixed carbonate-siliciclastic submarine canyon system, Great Barrier Reef margin, North-Eastern Australia. Mar. Geol. 289, 100–116.

Puga-Bernabéu, Á., Webster, J.M., Beaman, R.J., 2013a. Potential collapse of the upper slope and tsunami generation on the Great Barrier Reef margin, North-Eastern Australia. Nat. Hazards 66, 557–575.

Puga-Bernabéu, Á., Webster, J.M., Beaman, R.J., Guilbaud, V., 2013b. Variation in canyon morphology on the Great Barrier Reef margin, North-Eastern Australia: the influence of slope and barrier reefs. Geomorphology 191, 35–50.

Puga-Bernabéu, Á., Webster, J.M., Beaman, R.J., Reimer, P.J., Renema, W., 2014. Filling the gap: a 60 ky record of mixed carbonate-siliciclastic turbidite deposition from the Great Barrier Reef. Mar. Pet. Geol. 50, 40–50.

Puga-Bernabéu, Á., Beaman, R.J., Webster, J.M., Thomas, A.L., Jacobsen, G., 2017. Gloria Knolls Slide: a prominent submarine landslide complex on the Great Barrier Reef margin of North-Eastern Australia. Mar. Geol. 385, 68–83.

Puga-Bernabéu, Á., Webster, J.M., Beaman, R.J., Thran, A., López-Cabrera, J., Hinestrosa, G., Daniell, J., 2020. Submarine landslides along the mixed siliciclastic-carbonate margin of the Great Barrier Reef (Australia). In: Ogata, K., Festa, A., Pini, G.A. (Eds.), Submarine Landslides: Subaqueous Mass Transport Deposits from Outcrops to Seismic Profiles, American Geophysical Union, Geophysical Monograph, 246, pp. 313–337. Chapter 19.

R Development Core Team, 2020. R: a language and environment for statistical computing. ISBN 3-900051-07-0, URL. R Foundation for Statistical Computing, Vienna, Austria. http://www.R-project.org.

Scheidegger, A.E., 1973. On the prediction of the reach and velocity of catastrophic landslides. Rock Mech. 5, 231–236.

Schnyder, S.D., Eberli, G.P., Kirby, J.T., Shi, F., Tehranirad, B., Mulder, T., Ducassou, E., Hebbeln, D., Wintersteller, P., 2016. Tsunamis caused by submarine slope failures along western Great Bahama Bank. Sci. Rep. 6, 35925. https://doi.org/10.1038/srep35925.

Skempton, A.W., Hutchinson, J.N., 1969. Stability of natural slopes and embankment foundations. State-of-the-art report. In: Proceedings of the 7th International Conference on Soil Mechanics and Foundation Engineering, Sociedad Mexica de Mecánica de Suelos, Mexico City, vol. 2, pp. 291–335.

Solheim, A., Berg, K., Forsberg, C.F., Bryn, P., 2005. The Storegga Slide complex: repetitive large scale sliding with similar cause and development. Mar. Pet. Geol. 22, 97–107.

Staron, L., Lajeunesse, E., 2009. Understanding how volume affects the mobility of dry debris flows. Geophys. Res. Lett. 36, L12402. https://doi.org/10.1029/2009GL038229.

Symonds, P.A., Davies, P.J., Parisi, A., 1983. Structure and stratigraphy of the Central Great Barrier Reef. BMR J. Aust. Geol. Geophys. 8, 277–291.

Tanyas, H., Van Westen, C.J., Allstadt, K.E., Jibson, R.W., 2019. Factors controlling landslide frequency–area distributions. Earth Surf. Process. Landf. 44, 900–917. https://doi.org/10.1002/esp.4543.

Taylor, L.W.H., Falvey, D.A., 1977. Queensland Plateau and Coral Sea Basin: stratigraphy, structure and tectonics. APEA J. 17, 13–29.

ten Brink, U.S., Geist, E.L., Andrews, B.D., 2006. Size distribution of submarine landslides and its implication to tsunami hazard in Puerto Rico. Geophys. Res. Lett. 33, L11307 https://doi.org/10.1029/2006GL026125.

ten Brink, U.S., Barkan, R., Andrews, B.D., Chaytor, J.D., 2009a. Size distributions and failure initiation of submarine and subaerial landslides. Earth Planet. Sci. Lett. 287, 31–42.

ten Brink, U.S., Lee, H.J., Geist, E.L., Twichell, D., 2009b. Assessment of tsunami hazard to the U.S. East Coast using relationships between submarine landslides and earthquakes. Mar. Geol. 264, 65–73.

ten Brink, U.S., Andrews, B.D., Miller, N.C., 2016. Seismicity and sedimentation rate effects on submarine slope stability. Geology 44, 563–566.

Tilbrook, B., Matear, R., 2009. In: CSIRO (Ed.), Carbon Chemistry of the Great Barrier Reef. CSIRO Marine National Facility, Hobart, Australia, p. 17.

Twichell, D.C., Chaytor, J.D., ten Brink, U.S., Buczkowski, B., 2009. Morphology of late Quaternary submarine landslides along the U.S. Atlantic continental margin. Mar. Geol. 264, 4–15.

Urgeles, R., Camerlenghi, A., 2013. Submarine landslides of the Mediterranean Sea: trigger mechanisms, dynamics, and frequency-magnitude distribution. J. Geophys. Res. Earth Surf. 118, 2600–2618.

Vanneste, M., Mienert, J., Bünz, S., 2006. The Hinlopen Slide: a giant, submarine slope failure on the northern Svalbard margin, Arctic Ocean. Earth Planet. Sci. Lett. 245, 373–388.

Völker, D.J., 2010. A simple and efficient GIS tool for volume calculations of submarine landslides. Geo-Mar. Lett. 30, 541–547.

Völker, D.J., Scholz, F., Geersen, J., 2016. Morphometric parameters and outlines of 62 landslides off Central Chile. PANGAEA. https://doi.org/10.1594/PANGAEA.868892.

Watts, K.F., Varga, L.L., Feary, D.A., 1993. Origins, timing, and implications of Miocene to Pleistocene turbidites, debris flows, and slump deposits of the Queensland Trough, northeastern Australia (Site 823). In: McKenzie, J.A., Davies, P.J., Palmer-Julson, A., Sarg, J.F. (Eds.), Proceedings of the Ocean Drilling Program, Scientific Results, Vol. 133. Ocean Drilling Program, College Station, Texas, U.S.A, pp. 379–445.

Webster, J.M., Davies, P.J., 2003. Coral variation in two deep drill cores: significance for the Pleistocene development of the Great Barrier Reef. Sediment. Geol. 159, 61–80.

Webster, J.M., Davies, P.J., Beaman, R.J., Williams, S., Byrne, M., 2008. In: CSIRO (Ed.), Evolution of Drowned Shelf Edge Reefs in the GBR: Implications for Understanding Abrupt Climate Change, Coral Reef Response and Modern Deep Water Benthic Habitats. CSIRO Marine National Facility, Hobart, Australia, p. 18.

Webster, J.M., Beaman, R.J., Puga-Bernabéu, Á., Ludman, D., Renema, W., Wust, R., George, N.P.J., Reimer, P.J., Jacobsen, G.E., Moss, P., 2012. Late Pleistocene history of turbidite sedimentation in a submarine canyon off northern Great Barrier Reef, Australia. Palaeogeogr. Palaeoclimatol. Palaeoecol. 331–332, 75–89.

Webster, J.M., George, N.P.J., Beaman, R.J., Hill, J., Puga-Bernabéu, Á., Hinestrosa, G., Abbey, E.A., Daniell, J., 2016. Submarine landslides on the Great Barrier Reef shelf edge and upper slope: a mechanism for generating tsunamis on the north-east Australian coast? Mar. Geol. 371, 120–129.

Wilson, C.K., Long, D., Bulat, J., 2004. The morphology, setting and processes of the Afen Slide. Mar. Geol. 213, 149–167.